ERDC/CRREL TR-20-10

US Army Corps
of Engineers®
Engineer Research and
Development Center

ERDC
ENGINEER RESEARCH & DEVELOPMENT CENTER

Spatial and Temporal Variance in the Thermal Response of Buried Objects

Jay L. Clausen, Jason R. Dorvee, Anna Wagner, Susan Frankenstein, Blaine F. Morriss, Keran J. Claffey, Terrance M. Sobecki, Christopher R. Williams, Stephen D. Newman, Brandon K. Booker, Rosa T. Affleck, Charles E. Smith, Michele L. Maxson, Andrew P. Bernier, and Bonnie J. Jones

August 2020

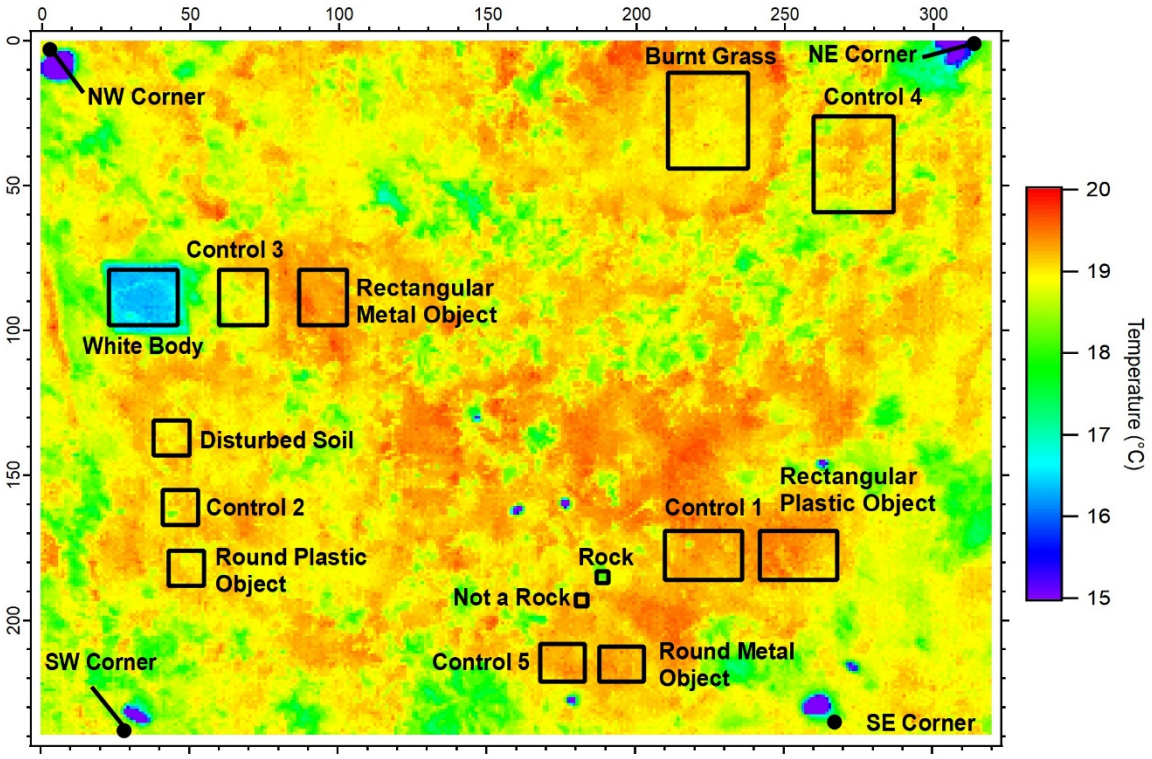

Cold Regions Research and Engineering Laboratory

The U.S. Army Engineer Research and Development Center (ERDC) solves the nation's toughest engineering and environmental challenges. ERDC develops innovative solutions in civil and military engineering, geospatial sciences, water resources, and environmental sciences for the Army, the Department of Defense, civilian agencies, and our nation's public good. Find out more at www.erdc.usace.army.mil.

To search for other technical reports published by ERDC, visit the ERDC online library at https://erdclibrary.on.worldcat.org/discovery.

ERDC/CRREL TR-20-10
August 2020

Spatial and Temporal Variance in the Thermal Response of Buried Objects

Jay L. Clausen, Jason R. Dorvee, Anna Wagner, Susan Frankenstein, Blaine F. Morriss, Keran J. Claffey, Terrance M. Sobecki, Christopher R. Williams, Stephen D. Newman, Brandon K. Booker, Rosa T. Affleck, Charles E. Smith, Michele L. Maxson, Andrew P. Bernier, and Bonnie J. Jones

U.S. Army Engineer Research and Development Center (ERDC)
Cold Regions Research and Engineering Laboratory (CRREL)
72 Lyme Road
Hanover, NH 03755-1290

Final Report

Prepared for U.S. Army
Communications-Electronics Research, Development, and Engineering Center
Night Vision and Electronic Sensors Directorate
Fort Belvoir, VA 22060

Under PE 622784 / Project T40 / Task A1040, “Analysis of Multimodal Sensors”

Abstract

Probability of detection and false alarm rates for current military sensor systems used for detecting buried objects are often unacceptable. One approach to increasing sensor performance and detection reliability is to better understand which physical processes are dominant under certain environmental conditions. Incorporating this understanding into detection algorithms will improve detection performance.

Our approach involved studying a small, 3.05 × 3.05 m, test plot at the Engineer Research and Development Center's Cold Regions Research and Engineering Laboratory (ERDC-CRREL) in Hanover, New Hampshire. There we monitored a number of environmental variables (soil temperature moisture, and chemistry as well as air temperature and humidity, cloud cover, and incoming solar radiation) coupled with thermal infrared and electro-optical image collection. Data collection occurred over 4 months with measurements made at 15 minute intervals.

Initial findings show that significant spatial and thermal temporal variability is caused by incoming solar radiation; meteorologically driven surface heat exchange; and subsurface-soil temperatures, density, moisture content, and surface roughness.

Contents

Figures and Tables

Figures

Tables

Preface

This study was conducted for the U.S. Army Combat Capabilities Development Command C5ISR Center under PE 622784 / Project T40 / Task A1040, "Analysis of Multimodal Sensors." The program monitor was Mr. Peter Brigham.

The work was performed by the Biogeochemical Sciences Branch (Dr. Justin B. Berman, Chief), the Terrestrial and Cryospheric Sciences Branch (Dr. John W. Weatherly, Chief), the Engineering Resources Branch (Mr. Jared Oren, Chief), the Force Projection and Sustainment Branch (Mr. J. D. Horne, Acting Chief), and the Signature Physics Branch (Dr. Marino A. Niccolai, Chief) of the Research and Engineering Division (Mr. J. D. Horne, Chief) and the Terrain and Ice Engineering Group (Mr. Stephen Newman, Lead) of the Remote Sensing / GIS Center of Expertise (Mr. David C. Finnegan, Chief), U.S. Army Engineer Research and Development Center (ERDC), Cold Regions Research and Engineering Laboratory (CRREL). At the time of publication, Dr. Bert Davis was the Technical Director for Geospatial Research and Engineering/Military Engineering. The Deputy Director of ERDC-CRREL was Mr. David B. Ringelberg, and the Director was Dr. Joseph L. Corriveau.

COL Teresa A. Schlosser was the Commander of ERDC, and Dr. David Pittman was the Director.

Acronyms and Abbreviations

ANOVA	Analysis of Variance
bgs	Below Ground Surface
CL	Lean Clay
CRREL	U.S. Army Cold Regions Research and Engineering Laboratory
CV	Coefficient of Variation
DF	Degrees of Freedom
ERDC	Engineer Research and Development Center
FAR	False Alarm Rates
FoV	Field of View
GPR	Ground-Penetrating Radar
GPS	Global Positioning System
HSD	Honest Significant Difference
IR	Infrared
LWTS	Light Weapon Thermal Site
MS	Mean of Squares
ppm	Parts per Million
RH	Relative Humidity
SD	Standard Deviation
SM	Silty Sand
SP-SM	Poorly Graded Sand with Silt
SS	Sum of Squares
UAV	Unmanned Aerial Vehicle
UGV	Unmanned Ground Platforms
VWC	Volumetric Water Content
XRF	X-Ray Fluorescence

1 Introduction

The environmental phenomenological properties responsible for the thermal variability in thermal infrared (IR) (0.7–13 μm*) sensor systems are complicated. This inability to account for environmental effects manifests in a poor probability of detection and elevated false alarm rate (FAR) when using IR for buried-object detection. Understanding the variables composing the thermal variance and associated IR signature would be invaluable in improving the signal-to-noise ratio for buried-object detection and reducing false alarms using IR sensors.

The U.S. Army has been testing a variety of sensor systems (IR, seismic, acoustic, radar, and electromagnetic) for detecting buried objects. It has also spent the last several years developing and testing a diversity of computer algorithms to improve buried-object detection. However, these efforts do not yet meet the performance necessary for a high-confidence system due to an inability to extrapolate what we know about soil and atmospheric phenomenological properties into generally useful detection tools (S. Howington, ERDC, pers. comm., 2020).

The Army needs techniques for rapidly assessing within a large spatial area the location of soils disturbed by buried-object emplacement. Coupling wide-area-assessment technologies, such as IR signatures, magnetic fields, or other spectroscopic sensor modalities on areal platforms, with novel geospatial statistical methods is a way to effectively evaluate large spatial areas for soil disturbances. Our approach uses mid- and longwave IR imagery for detecting soil disturbances. For example, modern thermal sensors are capable of detecting thermal differences of a fraction of a Celsius degree. However, a common problem for practical use of this technology is the elevated rate of false positive detections, which requires substantial human reanalysis.

* For a full list of the spelled-out forms of the units of measure used in this document, please refer to *U.S. Government Publishing Office Style Manual*, 31st ed. (Washington, DC: U.S Government Publishing Office, 2016), 248–252, https://www.govinfo.gov/content/pkg/GPO-STYLEMANUAL-2016/pdf/GPO-STYLEMANUAL-2016.pdf.

1.1 Background

Historically, electromagnetic sensor systems have been utilized to detect buried ferrous objects. However, buried objects are made out of a variety of materials (e.g., plastic and wood) besides metal. There is increased interest in other sensor modalities (e.g., IR hyperspectral imagery, seismic, acoustic, and ground penetrating radar [GPR]), which are all capable of detecting buried objects regardless the material composition. These sensor modalities are principally operated independently. However, the sensor application community has been exploring ways to fuse multiple sensor systems into a single comprehensive platform, allowing for complimentary integrative analysis (Chair and Varshney 1986). Additionally, using autonomous unmanned aerial vehicles (UAVs) or unmanned ground platforms (UGVs) could allow for quick characterization of an area from a distance.

The ability to accurately detect buried objects remotely is important for the Army, and interest in IR as a sensor modality has risen in the past decade (Kylili 2014). Thermal IR is based on the concept that the thermal signature of soil may be altered by objects buried at shallow depths within the soil (Moukalled et al. 2006). The technique measures surface-emitted electromagnetic energy in the IR radiation band, also known as thermal radiation. Materials differ in thermal capacities, resulting in different heating and cooling rates and associated IR emissions (Simard 1996). Buried-object detection using IR depends on the object's thermal signature being different than the surrounding soil. The deeper the object is buried, the more important it becomes to understand the soil signature and how it is affected by soil texture, water content, and other factors (Hong et al. 2002; De Jong et al. 1999). Other environmental factors investigated include diurnal cycles, numerical simulations, and meteorological properties (Pregowski et al. 2000; Sendur and Baertlein 2000; Simard 1996).

One readily acknowledged challenge in the use of IR for anomaly detection is the heterogeneous nature of soils (Carson and Salvaggio 2015; Moukalled et al. 2006). This can mask the signature of buried objects due to the high variability of the thermal emissions of the soil itself. A host of environmental factors affect soil IR signatures, such as surface-soil temperature and texture, moisture content, material density, and reflectance. However, the variability within these factors and their interactions are understood but unexploitable at the present. For instance, diurnal thermal fluctuations due to changing solar input throughout the day give rise to thermal contrasts at the soil surface (Khanafer and Vafai 2002; Van De

Griend et al. 1985). Adding to this complexity is the additional influence of a buried object on both heat and moisture transfer (Pan and Mahrt 1987).

Thermal imaging as a sensor modality increased in popularity in the early 2000s in an attempt to increase buried-object prediction and detection (Kylili 2014). The most common approach is to hold all but one soil property constant in hopes of seeing a discernable pattern in the data output as a result of varying the one factor. Van Dam et al. (2003) was the first to begin investigating the effect of soil properties and meteorological forcing on buried-object detection. They discovered that for two soils tested under both dry and wet conditions, soil texture had a large influence on the thermal signature of a buried object. However, the two soils had very similar thermal properties dry (thermal conductivity of 0.25 vs. 0.29) and wet (2.18 vs. 1.59). Further, the surface expression of many small buried targets was unobservable unless they were at a shallow depth below the surface. Van Dam et al. (2003) also concluded that the water content affected the thermal signature. Both the temperature effect and lag were predictable.

Koenig et al. (2008) stated that accounting for the properties of disturbed and undisturbed soil can improve detection of buried objects. Khanafer et al. (2003) believed that the presence of a buried object disturbs the heat and diffusion parameters of the surrounding soil, enabling anomaly detection. However, it now is generally believed that it is the disturbance of the soil and alteration of the soil properties that gives rise to the thermal signature. Thermal contrasts are manifested as a result of three effects: (1) the object itself likely has different thermal properties than the soil it has replaced, which may result in differential heat transport and a thermal expression at the surface; (2) disturbing a soil normally changes its density and thermal properties, also leading to a surface expression of physical temperature; and (3) disturbing a soil redistributes finer particles to the ground surface, which, for some soil compositions, changes their spectral reflectance (S. Howington, pers. comm., 2020). The surface effect remains for weeks after the disturbance and enhances the contrast induced by the buried object.

Waldemar et al. (2012) extended the work of Hong et al. (2002) and Van Dam et al. (2003). They used physical measurements and numerical modeling techniques to observe the effects that varying moisture levels and the density of soil have on buried-object detection. Predicting expected surface temperatures is complicated by the nonlinear movement of water within

soil and changes in surface temperature during the drying process. Understanding the relationship between meteorological conditions and soil properties is paramount to detect objects buried in soil and to predict sensor performance. However, an in depth review of the soil science, agricultural, and atmospheric literature may shed more light on understanding the near surface processes.

1.2 Objectives

This research aimed to better understand the environmental (soil and atmospheric) phenomenological properties affecting temporal and spatial thermal variance of soils. We explored how to quantify the natural variance such that it can be subtracted from a disturbed area signal by accounting for the physical phenomenological material and atmospheric properties.

1.3 Approach

To meet the project objectives, we developed the Cold Regions Research and Engineering Laboratory (CRREL)/C5ISR Test Bed, which consisted of an instrumented volume of soil containing various sizes, types, and materials of buried objects monitored with a thermal IR sensor. This allowed us to test and validate our understanding of the physical properties responsible for soil temporal and spatial variance.

2 Methods

2.1 Test layout

The test plot was located at CRREL in an area devoid of brush and trees, minimizing shadow effects (Figure 1). This study consisted of two 3.05 × 3.05 m test plots, each containing twenty-five 61 × 61 cm cells. One test plot was scraped with a surface excavator to remove the surface vegetation, exposing bare ground (consisting of mineral soil) to simulate a typical unsurfaced road (Figure 2). The second test plot was constructed with a grass strip down the middle (partial bare). A separate future report will discuss the results from this second plot.

Figure 1. Area of the CRREL test plots.

Figure 2. Test plot showing the grid outline before object emplacement.

We placed foil-covered rocks, fiducials, at the four corners of the test plot as clearly discernable markers to enable georegistration of the plot imagery. Fiducials reflect the cold sky and are used as a quality control check for proper camera function. They provide an estimate of background reflected radiation and are always much colder than the surrounding soil surface.

2.2 Object emplacement

On 6 October 2016, we buried several objects at the test plot following guidelines in U.S. Army (2004). A small excavation was made to a depth sufficient to cover the buried object with 5 cm of soil. The removed soil was placed on plastic next to the hole and then used to cover the object.

Figure 3 shows the object emplacement and naming convention. The objects were placed in the following cells: a Round Plastic object in cell B4 (note that Figure 3 shows the object in B3), a Rectangular Metal object filled with ammonia nitrate fertilizer in cell B7, a Rectangular Plastic object filled with ammonia nitrate fertilizer in cell B24, and a Round Metal object in cell B20. To test the effect of soil disturbance without object emplacement, the soil in cell B3 was disturbed, but no object was placed. A whitebody panel was installed at the test plot in cell B2. It was not buried but remained on the surface and is used for camera calibration. It is hereafter referred to as the whitebody. Figure 4 provides a reference when discussing the IR images and the emplacement of each object and corresponding control area.

Figure 3. Object emplacement with grid naming convention.

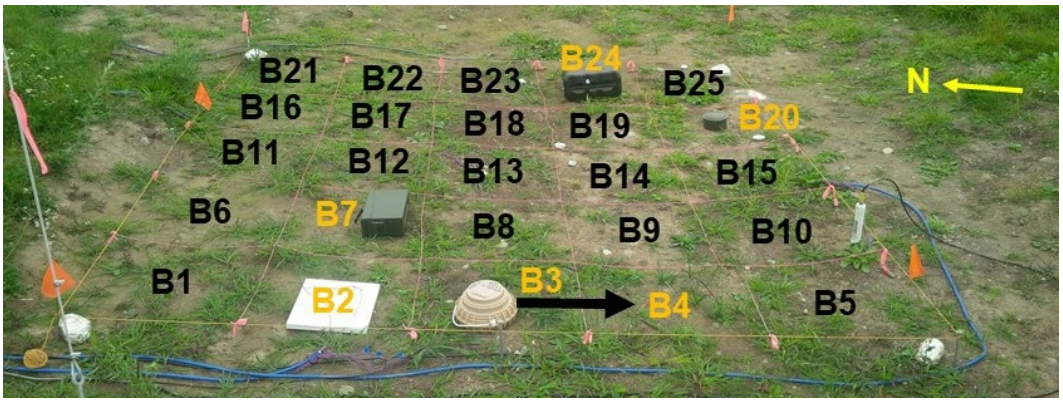

Figure 4. Spatial locations of buried objects, disturbed soil, whitebody panel, fiducials, and control areas for the CRREL 3.05 × 3.05 m test plot.

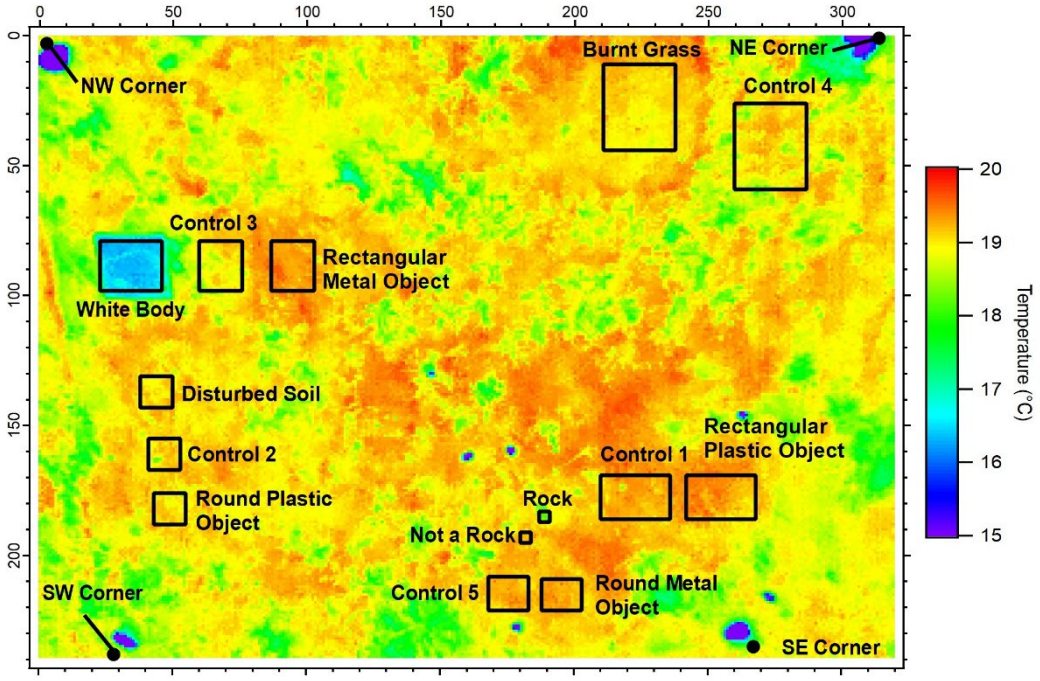

2.3 Meteorological measurements

The meteorological station was located approximately 50 m towards the south from the plots. It had upward- and downward-looking radiometers to record incoming and reflected solar radiation. These radiometers provide gross limits of the energy balance against which measured camera-pixel intensities can be evaluated. They also allow calculation of the average reflected and incoming solar albedo. The meteorological station recorded air temperature (approximately 1 m above the ground), precipitation, wind speed and direction, barometric pressure, and relative humidity. Data acquisition was at 15-minute intervals and synchronized to the thermal IR camera.* Data acquisition began on 30 August and continued to 31 December 2016. Appendix A (Table A-3Table A-3) provides a complete list of the meteorological instrumentation and operational parameters.

For further background radiation assessment, we installed two downward-looking radiometers in the plot area, one observing bare soil, the other a vegetated area. These provided measurements of outgoing longwave radiation synchronized to the camera data collections. At night, these represent

* Going forward, we refer to the thermal IR camera as simply an IR camera.

emitted terrestrial longwave IR; during the day, they incorporate a significant reflected component forming part of the background.

2.4 Surface characterization

Surface topography was measured using Riegl's VZ400 lidar. Each scan position consisted of one overview scan that was collected with a theta start angle of 30°, a theta stop angle of 130° (vertical range), and the full 360° phi angle (horizontal). For the overview scan, the resolution was 0.06° in both the horizontal and vertical and a 300 kHz pulse repetition rate. Tie points for the scans were a mixture of 5 cm flat circular reflectors and 10 cm cylindrical reflectors. Once overview scans and reflectors were scanned, the test plot was imaged using a high-resolution scan, 0.015° resolution in both the horizontal and vertical, at a 300 kHz pulse repetition rate. All scans were georegistered using both GPS (Global Positioning System) coordinates and reflector root mean square fitting. The scans were further corrected using multistation adjustment to minimize the error between scans.

2.5 Soil characterization

2.5.1 Particle size

Our study collected soil samples at various depths. Grain-size analysis followed the ASTM D422 method (ASTM 2007).

2.5.2 Soil density

We used two methods to measure the density of the in situ soil; these included the drive cylinder and an eGauge, a Troxler Model 4590 surface density gauge. It measures the in situ density and gravimetric water content at 5.1 cm intervals to 20.3 cm to give both the wet and dry densities. The drive cylinder measurements provided full-depth characterization by manually pushing a 4.5 cm diameter and 6 cm high cylinder into the soil; the soil sample was then retrieved, weighed, and placed to dry in the oven.

2.5.3 Soil chemistry

The metal content of a soil sample obtained from the center of each grid was analyzed using x-ray fluorescence (XRF). XRF analysis involved using an Innov-X Model System A-4000 alloy metals analyzer with the M4000S

soil analysis package and electron tube. The detection limit of the instrument varies by analyte from approximately 10 to 50 ppm (parts per million). The analytes included Ag, As, Co, Cr, Cu, Fe, Mn, Mo, Ni, Pb, Sb, Yi, and Zn.*

2.6 In situ instrumentation

We installed in the test plot in situ devices for measuring soil temperature, volumetric water content, bulk electrical conductivity, and relative dielectric permittivity (Figure 5). The appendix (Table A-3) lists specifications of the equipment. Table A-1 and Table A-2 of the appendix give exact locations and naming conventions.

Soil temperature was measured at five locations (Figure 5) within the plot using a string of thermocouples installed at six depth intervals: 0.0, 5.1, 15.2, 30.5, 45.7, and 61.0 cm† below ground surface (bgs). The thermocouples were fabricated and calibrated at CRREL. The measurable dynamic temperature range of the thermocouples is −27°C to 37°C; however, the maximum recorded temperature was limited to 35°C due to data acquisition restraints. At location B2 (see Figure 2) a thermocouple was placed on the surface of the whitebody.

Six calibrated Campbell Scientific CS655 sensors were installed at two locations (Figure 5). These sensors measure temperature, volumetric water content, bulk electrical conductivity, and relative dielectric permittivity. Two Campbell Scientific CS616 water content reflectometers were installed, one in the test plot (Figure 5) and one just northeast of the plot (not shown). The CS616 water content accuracy is 2% when calibrated to the surrounding soil.

Volumetric water content was measured at one location in the test plot (Figure 5) with a Delta-T PR2 soil moisture probe. The probe has sensing elements at 10.2, 20.3, 30.5, 40.6, 61.0, and 91.4 cm‡ bgs.

* For a full list of the spelled-out forms of the chemical elements used in this document, please refer to *U.S. Government Publishing Office Style Manual*, 31st ed. (Washington, DC: U.S Government Publishing Office, 2016), 265, https://www.govinfo.gov/content/pkg/GPO-STYLEMANUAL-2016/pdf/GPO-STYLEMANUAL-2016.pdf.

† These depths correspond to 0, 2, 6, 12, 18, and 24 in.

‡ This corresponds to 4, 8, 12, 16, 24, and 36 in.

Figure 5. Subsurface instrumentation emplacement.

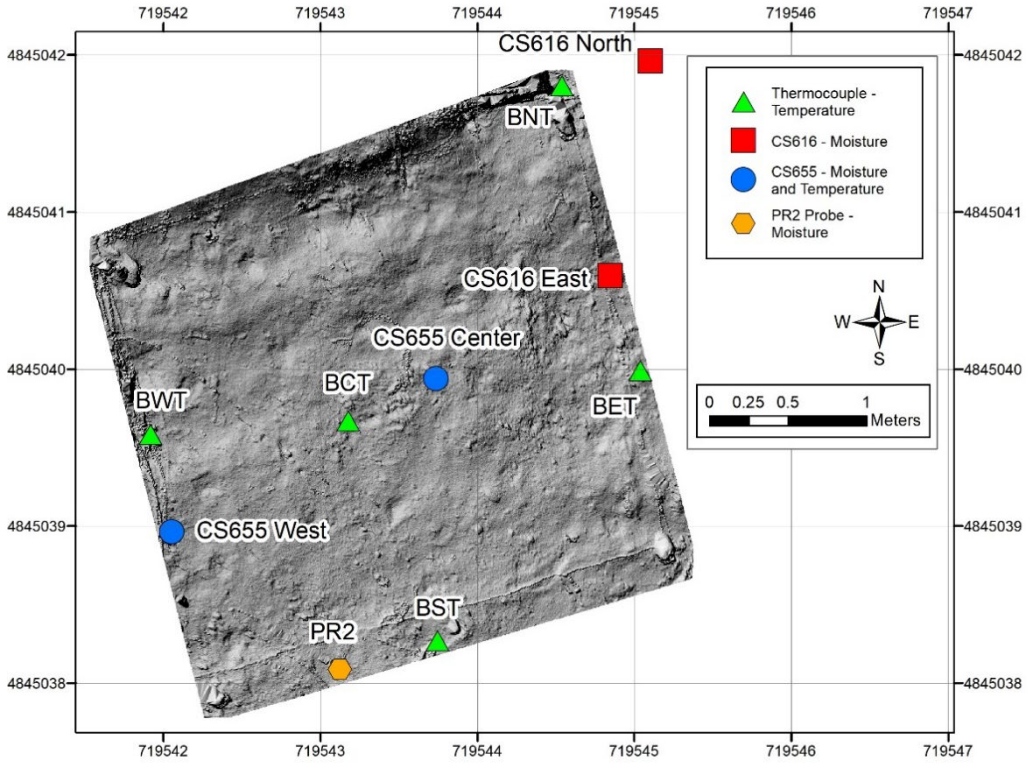

2.7 Thermal infrared (IR) sensors

The surface of the test plot was also characterized with sensors to measure surface roughness and the thermal properties in the visible-to-short-IR wavelengths. Thermal properties of the surface were collected using a heat flux sensor, short- and longwave radiometers, IR (Figure 6), and LWTS (Light Weapon Thermal Site) cameras. This report does not discuss the LWTS camera data. We used a field spectrometer to measure the visible-to-shortwave-IR signature of the surface. The plot was imaged using a FLIR Systems Inc. camera (model A300) with the Scout III 240 lens. Camera details are listed in Table A-3 of the appendix. The field of view is 24° × 18°, which covers the entire 3.05 × 3.05 m plot. The camera's resolution is 320 × 240 pixels with a spatial resolution of 25 μm for the 24° lens using an uncooled microbolometer. The camera provides fully radiometric 16-bit real-time video to a computer.

Figure 6. The IR camera setup at the test plot.

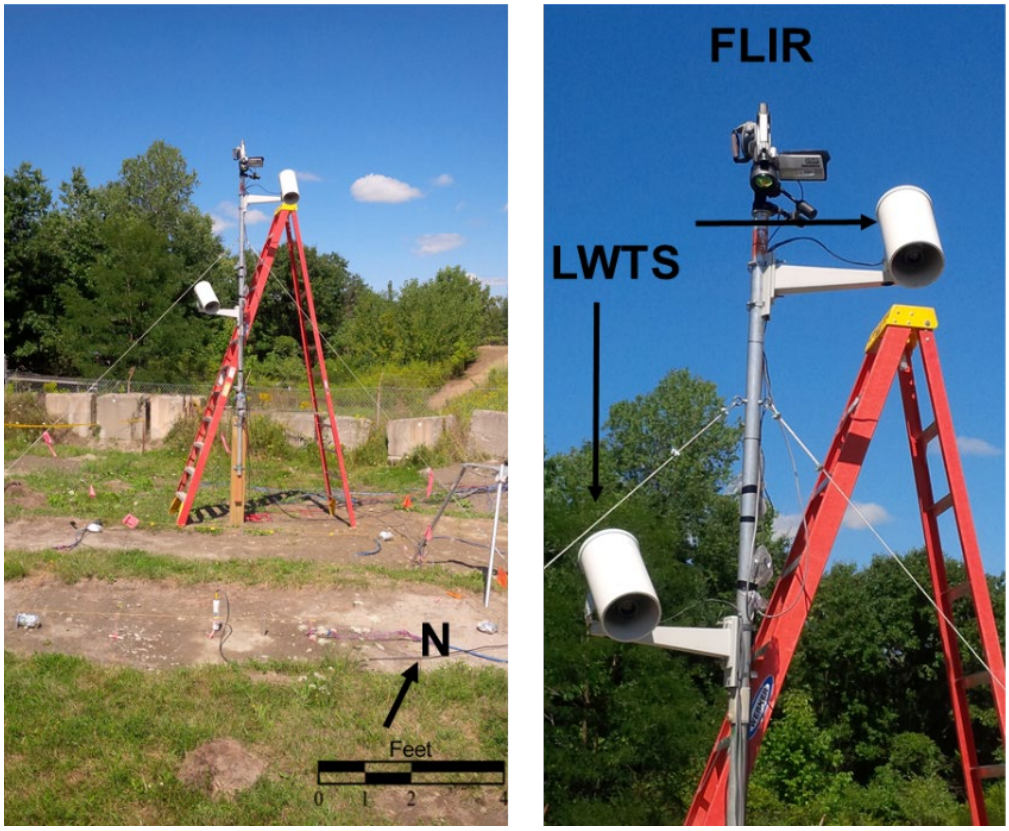

2.7.1 IR camera calibration

The IR camera outputs the intensity of the received radiation (energy per unit area per time). The raw intensity data is converted to temperatures by using either the FLIR software or by using the FLIR-supplied metadata and external tools. The IR camera output temperatures must be corrected for background radiation and emissivity difference effects to obtain a sensible-heat-temperature equivalent that equals the physical temperature. Before the camera was used, it was calibrated against measured soil temperatures and white- and blackbodies equilibrated to the surrounding atmospheric, and in some cases soil surface, temperature using a two-step process.

The first step involved verifying that the FLIR software was correctly converting the raw image radiance data files to temperatures. Using ExifTool (a UNIX program capable of reading, writing, and editing meta information from a wide variety of files, including proprietary imagery), the emissivity and reflected apparent temperature were extracted from each radiance file (three separate 8-bit band intensities or a composite 24-bit value in *.jpg format). These parameters were then input into MATLAB's

FLIR software development kit, which enables postprocessing of IR imagery to calculate the associated temperatures. These values were then compared to those calculated using the proprietary FLIR software.

The second step compared the calculated temperatures against several external probe reference temperatures using the following procedure:

1. At five locations within the test plot, we installed calibrated strings of thermocouples at various depths, extending from the surface down to 65 cm below the surface. Measurements were collected every 15 minutes. The adjacent field weather station provided the atmospheric temperature.

2. We placed white (high reflectivity) and black (highly absorptive) tiles in the plot and collected images of them.

3. We compared the relative temperature output of the IR camera to the imaged white- and blackbody temperatures to establish the difference between the two measurements.

4. We adjusted the IR camera results by varying the emissivity used by the IR analysis software to compute the temperatures from the spectral radiance values (i.e., the Stefan-Boltzmann equation).

The spectral concentration (i.e., intensity at a specific frequency or range of frequencies) of radiation emitted from an ideal blackbody emitter (i.e., no reflectance or transmission nor internal absorption of IR) is a function of temperature above absolute zero. This fact enables the use of IR radiometers for remote temperature measurement. As temperature increases, the radiation emitted from an object or area increases in intensity; and its wavelength distribution shifts towards shorter wavelengths. The total energy flux emitted from a blackbody as a function of temperature is quantified by the Stefan-Boltzmann equation:

$$W = \varepsilon \sigma T^4, \tag{1}$$

where

W = the radiant energy emission flux (W/m^2),
T = the absolute temperature (K),
ε = emissivity,
σ = the Stefan-Boltzmann constant, 5.6697×10^{-8} W/m^2·K^{-4}.

A perfect blackbody has an emissivity of 1. Most materials and objects behave as graybodies, or nonideal emitters, having an emissivity less than 1. In other words, they emit less radiation than an ideal blackbody per unit temperature at thermal equilibrium. The actual amount of radiation sensed using IR radiometers or thermometers is the sum of not only the emitted but also the transmitted and reflected background radiations. Application of the Stefan-Boltzmann equation to such materials results in underestimation of the true physical temperature. This temperature is known as the apparent, or "relative," temperature.

The true physical temperature can be approximated if the measured radiation is corrected for the above effects. Thus, the energy measured by the sensor is given as

$$\begin{aligned} E_s &= \varepsilon E_t + (1-\varepsilon)E_b, \\ \varepsilon\sigma T_s^4 &= \varepsilon\sigma T_t^4 + (1-\varepsilon)\sigma T_b^4, \end{aligned} \tag{2}$$

where

E_s = the radiant energy measured at the sensor;
E_t = the radiant energy from the target;
E_b = the radiant energy from the sky and reflected from other objects within the field of view;
T_s = the temperature measured by the sensor;
T_t = the target temperature;
T_b = the background temperature, usually taken to be the sky temperature; and
ε = the target emissivity.

On a clear day, the background surface-soil temperature will be much colder than the target; on a cloudy day, the two will be nearly the same.

A simple correction for emissivity difference between the target and an ideal blackbody emitter alone is to divide the temperature computed from the radiometer measurement by the object's emissivity. This adjusts the temperature upward and, although commonly used, is not correct as it fails to account for reflected radiation. The correction requires knowing, or estimating, the emissivity of the bodies, which is a function of their composition (Sutherland et al. 1979; Wiecek and Pacholik 1995). The software supplied with the IR camera has this capability. By postprocessing the collected image, one can make emissivity adjustments of a scene to arrive at a

relative temperature value that approximates actual temperature. A relative temperature is not, however, a calibrated temperature, which is tied back to a direct physical temperature measurement using more direct means (i.e., thermometry or pyrometry).

One question was the accuracy of the measured IR camera surface-soil temperatures. Comparison between four surface thermocouples and the IR-calculated temperatures indicated general agreement between the two and that they were consistent (Figure 7).

However, up to 10°C or more differences between the IR and thermocouple data occurred in some cases. This happened most often when surface-soil temperatures were in the 20°C–30°C range and higher. This was due in part to data acquisition limitations such that the maximum thermocouple temperature was 35°C. The slope of the lines between the IR and thermocouple data is less than the 1:1 ratio (Figure 7), indicating that the IR camera measured surface-soil temperatures are higher than direct thermocouple measurements.

Shading due to microtopographic surface roughness could result in underestimation of temperature by the thermocouples as compared to the IR camera. However, there is minimal relief at the test plot and some of the largest differences occur around solar noon. An individual thermocouple might be in a shaded position at some time during the day, while the IR measurements are surface-temperature estimates over a sampling of pixels (i.e., a 5 × 5 pixel matrix). Alternatively, the difference may be more related to the skin temperature measured by the IR camera versus a volumetric average temperature of the thermocouple (S. Howington, pers. comm., 2020). If the thermocouple is on the soil surface, direct loading occurs on the device. If it is beneath the surface, it will often be different than the soil's skin temperature because the gradient can be large in those first few top millimeters of soil. Consequently, the differences in temperature measurements may be related to the area being evaluated. The thermocouples are measuring the temperature of the soil in direct contact with the device. In contrast, the IR image for the thermocouple areas consists of approximately 25 pixels, which are averaged. Comparison of a direct measurement and an average value may explain this difference. It is also possible that the IR camera may be affected by the IR reflectance to a greater degree than the thermocouples, overestimating the real surface-soil temperature.

Figure 7. Comparison of four thermocouple strings and IR surface-soil temperatures. The lines are the best-fit linear representations. Equations are given for the two extremes.

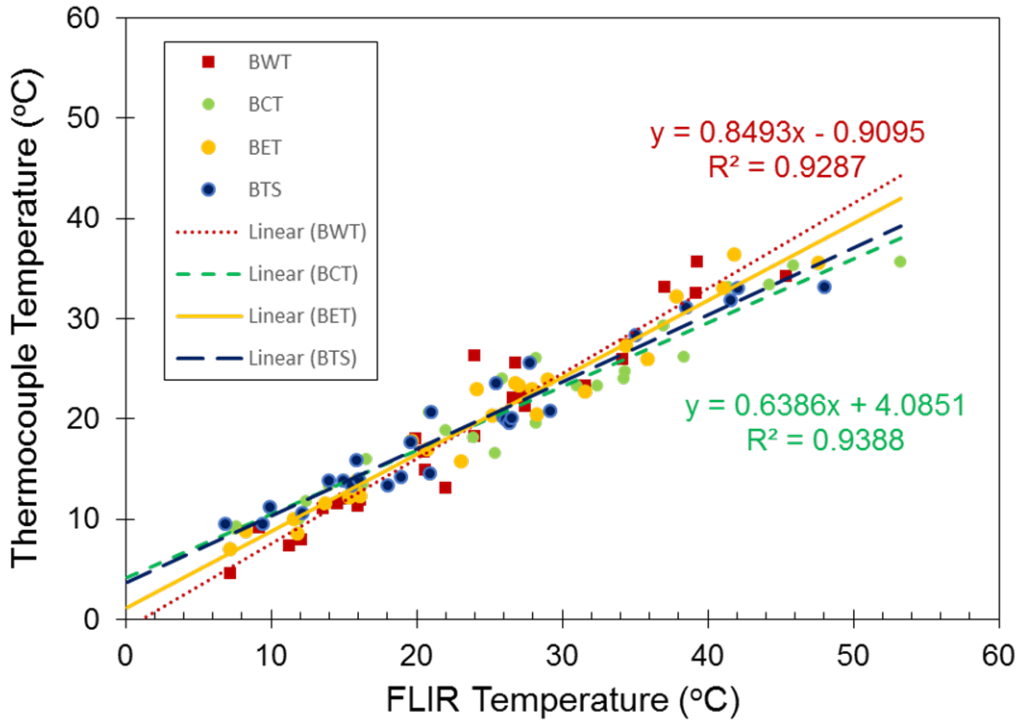

2.7.2 Georeferencing

The IR data collected is an estimation of the incident radiation at the sensor, subject to the spectral sensitivity, resolution, and field of view of each detector. The field of view (FoV), along with the distance between the sensor and the target, controls the pixel size of an image. It should be noted that each pixel in a "raw" image is an extrapolation of an essentially circular (hemispheric) signal mapped to a square. A pixel is, spatially, the fundamental unit of an image; and because its extent is a function of the sensor geometry, surface geometry, and FoV, each pixel's ground footprint is different.

Our IR camera was mounted at a height of 4.27 m on a tower approximately 1 m north of the test-plot boundary, resulting in oblique image views. The plot images are composed of square pixels that, in reality, do not represent square (or particularly similar) areas on the ground. However, the thermal images have a high enough resolution to accurately delineate the plot and subplots by using the ground strings that define their extent. The pixels represent an area of approximately 2 cm^2. Some error is incurred as the strings cut across pixels; but within the constraints of the imagery resolution and human judgment, the strings provide an accurate

method for determining which pixels in an image correspond to the plot or subplot.

An alternative method for attributing sensor data to the plot and subplots is to georeference the images, or warp them to some coordinate system (e.g., GPS coordinates). The success of this warping relies on sufficient characterization of the ground surface. At a minimum, the location of each corner of the plot is needed; at best, the corner coordinates of each pixel are required. In the latter scenario, pixels on the border between subplots are attributed to one of the subplots they overlap, achieving the same accuracy as the previous method; or they can be subdivided and averaged into the surrounding plots, resulting in an improved representation. Departure from planar geometry between the georeferenced pixels and the control points incurs error when defining the extent of the subplot. For the purpose of calculating subplot-level statistics from the thermal imagery, the project team decided that georeferencing the imagery first would degrade the quality of the image data.

Consequently, our primary approach was to work with nongeoreferenced IR image data so that the IR imagery quality was not unnecessarily degraded. In those instances where IR imagery at the pixel scale was directly compared to rasterized data (e.g., lidar data used for characterizing surface roughness or texture), georeferencing of the imagery was performed. To assist in georeferencing, a visible camera was installed at the test plot on 13 October 2016 on the same pole as the IR camera at a height of 4.27 m, capturing a field of view similar to the IR camera. Figure 8 is an example of a visible and IR image for the same point in time. In all subsequent figures, north is in the upward direction.

Figure 8. Visible and IR image on 14 October 2017 at 1100.

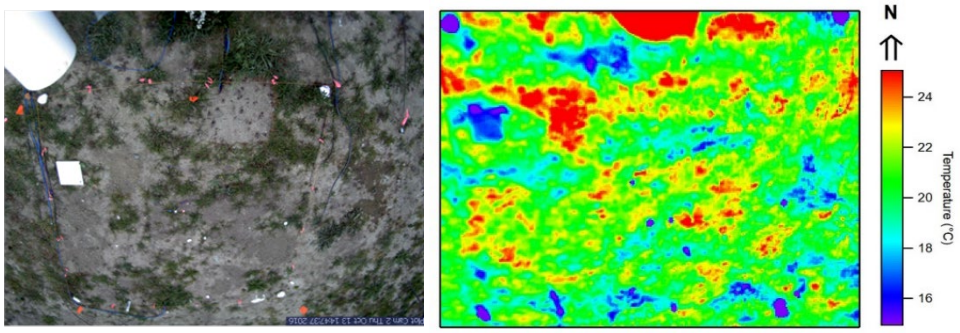

2.7.3 IR image keystoning

To compare the soil heat flux data directly with the IR images, the images need to be adjusted to better represent the relative square dimensions of the plot. As mentioned, the IR images were taken at an angle, which creates an optical perspective effect known as keystoning. This means that the top of the image and the bottom of the image do not have the same width and that the image itself is elongated with respect to the change in aspect ratio between the top and bottom of the image (Figure 9). In reality, the bright spots in the corners are essentially square to each other. This study used numerous orthorectification techniques to adjust the image to a fixed reference frame.

Figure 9. An example of keystoning of an IR image.

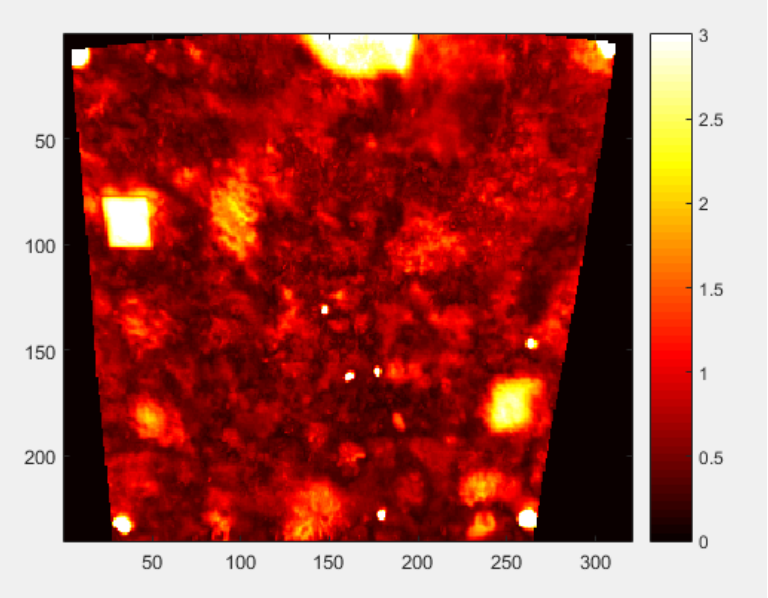

2.8 Statistical analysis

The best way to understand the interrelationship of two-dimensional spatially correlated spaces, especially thermal images and thermography, is to use spatial variograms. A variogram, denoted $2\gamma(x, y)$, of a set of spatially correlated observations at locations $\boldsymbol{s} = (s_1, s_2, \ldots, s_n)$ is defined as the variance of the difference between field values at two locations across all realizations of the field, given by the equation

$$2\gamma(s_i, s_j) = var\left(Z(s_i) - Z(s_j)\right), \quad (3)$$

where, for this study, $Z(s_i)$ is the observation of thermal temperature at spatial location s_i.* Since the variograms are theoretical quantities that cannot be observed in nature but are estimated from the data, the calculated values are more correctly referred to as empirical variograms.

A variogram is the most important tool in exploratory spatial analysis. The variogram measures the spatial autocorrelation of a field by describing how sample data are related with distance and direction. We can construct semivariograms of the thermal signatures of our test plot for any IR image recorded (Figure 10). The *sill* is the variance at which the curve starts to flatten, the *range* is the lag (distance) at which the sill occurs, and the *nugget* is the variance at which the variogram intersects the y-axis. All of the variograms presented in this report are of the spherical type, which is the most common form, meaning that a modified quadratic equation can be fit to the data to obtain the sill and range (solid lines shown in Figure 10).

Variogram graphics like Figure 10 allow us to see the spatial structure of the variability of the test plot and how that variability changes with time. Observing empirical semivariograms allows us to draw information that, in turn, allows us to begin to make inference about the thermography spatial structure.

Figure 10. Example of semivariograms of IR images generated from the CRREL test-plot data.

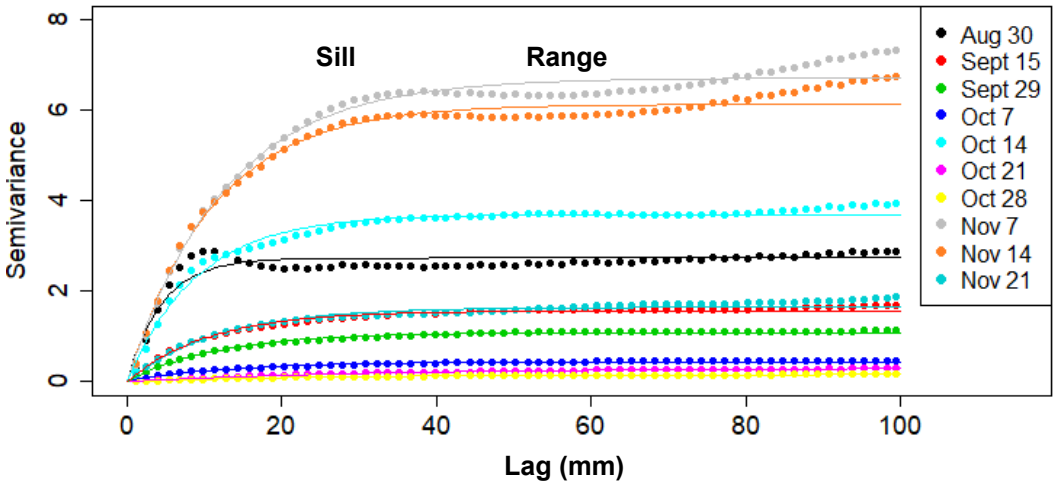

The statistical evaluation also consisted of an Analysis of Variance (ANOVA) test (one-way) and a Tukey Honest Significant Difference (HSD) test. The one-way ANOVA test compares two means from two independent

* A semivariogram is a variogram divided by two and is often used interchangeably with variogram. A semivariogram is denoted $\gamma(x, y)$

groups by using the F-distribution. The HSD test is a pair-wise comparison of difference of the means in reference to the standard error and is performed after the ANOVA test.

3 Results

Our results are separated into a predisturbance and postdisturbance period. The objects were placed in the test plot on 6 October 2016. The predisturbance results span from 30 August to 5 October 2016, and the postdisturbance results span from 6 October to 21 November 2016.

3.1 Surface characterization

A lidar survey conducted on 24 August 2016 obtained the surface roughness of the test plot. The undisturbed plot surface varied by less than 13 cm across the test plot (Figure 11). Aspect, slope, and hill shade maps were generated from the lidar surveys.

Figure 11. Topography of the test plot.

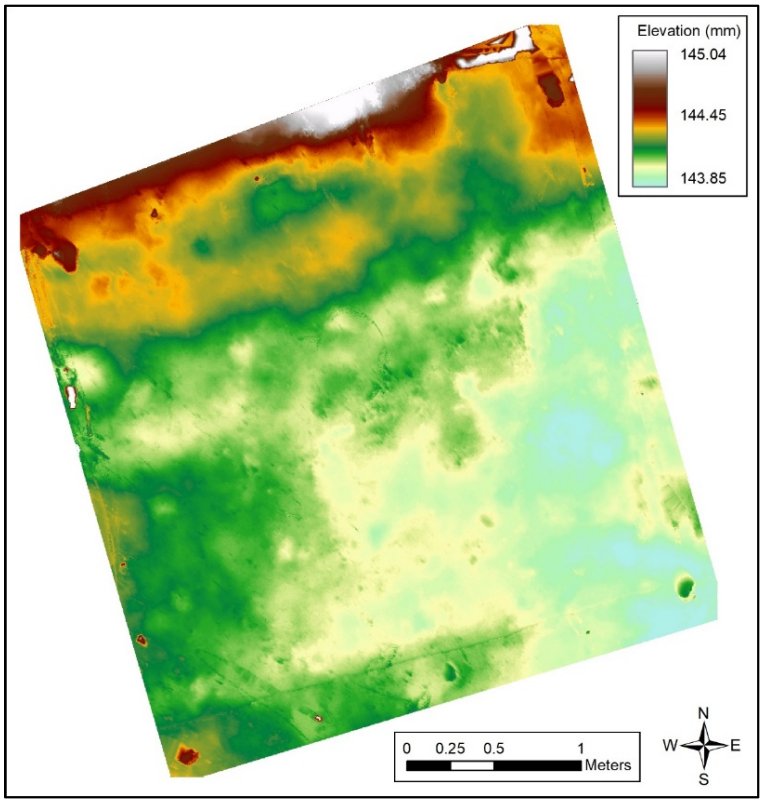

The aspect of the soil surface depicts the microtopography, which, for the test bed, is defined by a relatively flat surface with small undulations and pebbles (Figure 12). The slope of the soil surface (Figure 13) is generally less than 15%. The steeper slope areas represent cables on the soil surface or markers placed at the corners of the plot for orthorectification.

Figure 12. The aspect (degrees) of the test plot.

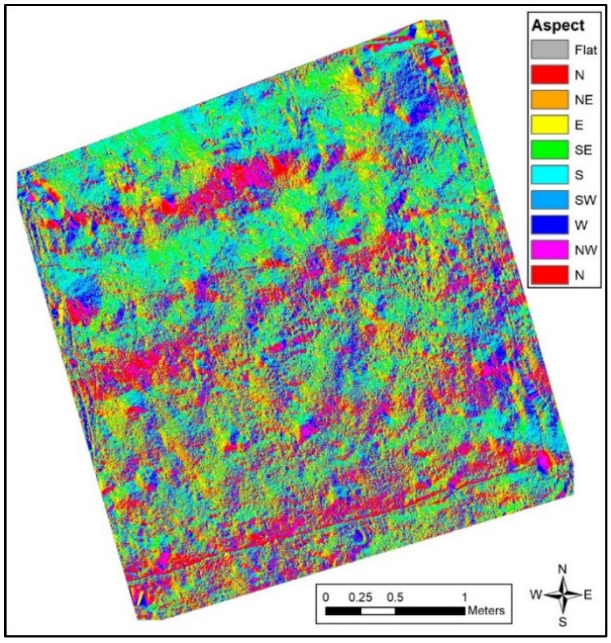

Figure 13. The slope (%) of the test-plot soil surface.

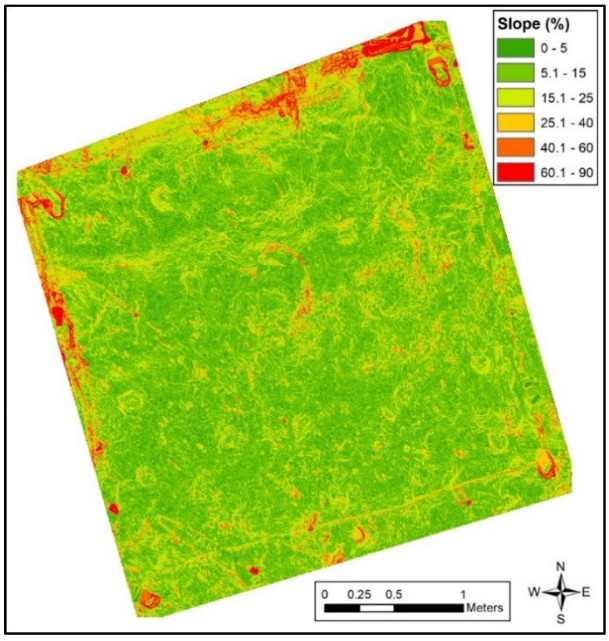

3.2 Meteorological properties

Localized meteorological data were collected contemporaneously with the IR and soil measurements. Figure 14 shows the meteorological conditions for September through November. Air temperature varied from 12°C to 26°C at the start of the data collection to −5°C to 21°C at the end (Figure 14*a*). The average air temperature for this time period was 10.3°C. For the

first month of the test period, the site was relatively dry with a few single-day precipitation events (Figure 14*b*). Following object placement (6 October), there were several heavy multiday precipitation events and one 24-hour event that alone totaled about 27 mm. The 22 and 27 October 2016 precipitation events resulted in temporary water ponding on the test-plot surface. Figure 14*c* shows a wind rose for that time period. The average wind speed for that time period was 0.7 m/s with a maximum of 3.8 m/s.

Figure 14. Meteorological conditions for September through November 2016: (*a*) Air temperature, (*b*) precipitation, and (*c*) wind velocity and direction.

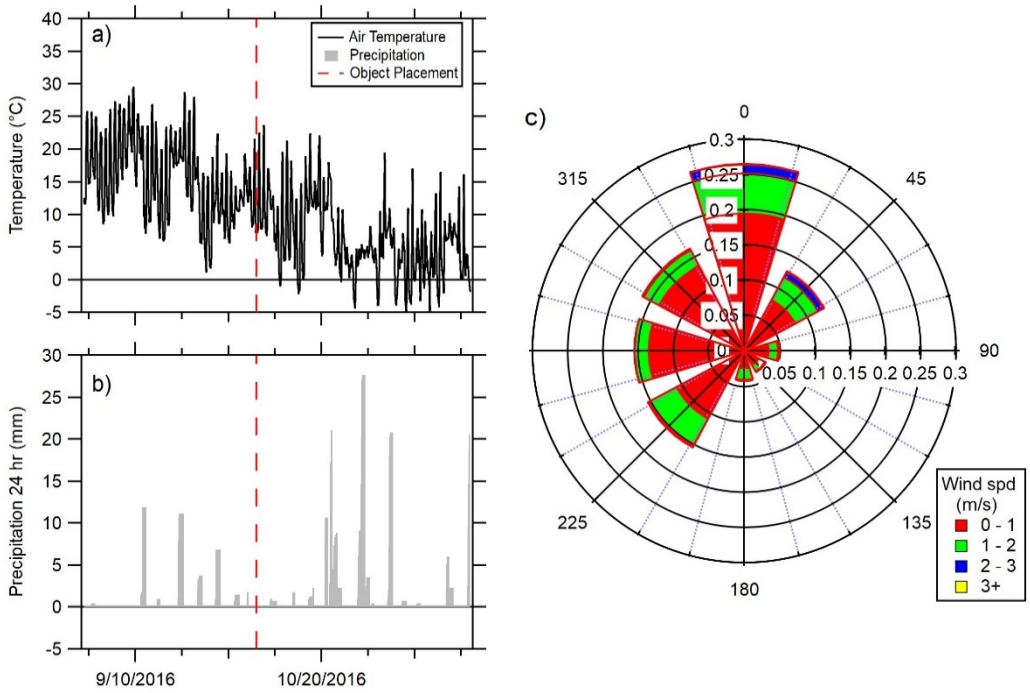

3.3 Incoming and outgoing radiation

Figure 15 shows the incoming solar radiation at the meteorological station and the reflected and emitted longwave (4 to 50 μm) and reflected shortwave (0.285 to 2.8 μm) radiation. A diurnal cycle is evident in the data, consistent with the day/night cycle with peak radiation occurring at noon. Peak incoming shortwave radiation was approximately 900 W/m² on 30 August 2016 with a general decline of roughly 200 W/m² during the period of interest, reflecting the lower sun angle going from summer to fall in the northern hemisphere. Significantly lower incoming radiation is associated with cloudy days with a thick cloud deck. A similar diurnal trend is evident for short- and longwave outgoing radiation. The peak shortwave reflected radiation is approximately 150 W/m², and longwave reflected

and emitted radiation ranges from approximately 350 to 550 W/m² for this measurement period. A close-up view of the radiometer data from 14 to 19 September 2016 (Figure 15*b*) shows that the peak long- and shortwave outgoing radiation occurs approximately 1 hour after the maximum incoming shortwave radiation.

Figure 15. Incoming shortwave radiation (*red*), surface-reflected shortwave radiation (*blue*), and reflected and emitted longwave radiation (*black*) (W/m²) for (*a*) 30 August 2016 to 21 November 2016 and (*b*) 14 September 2016 to 19 September 2016.

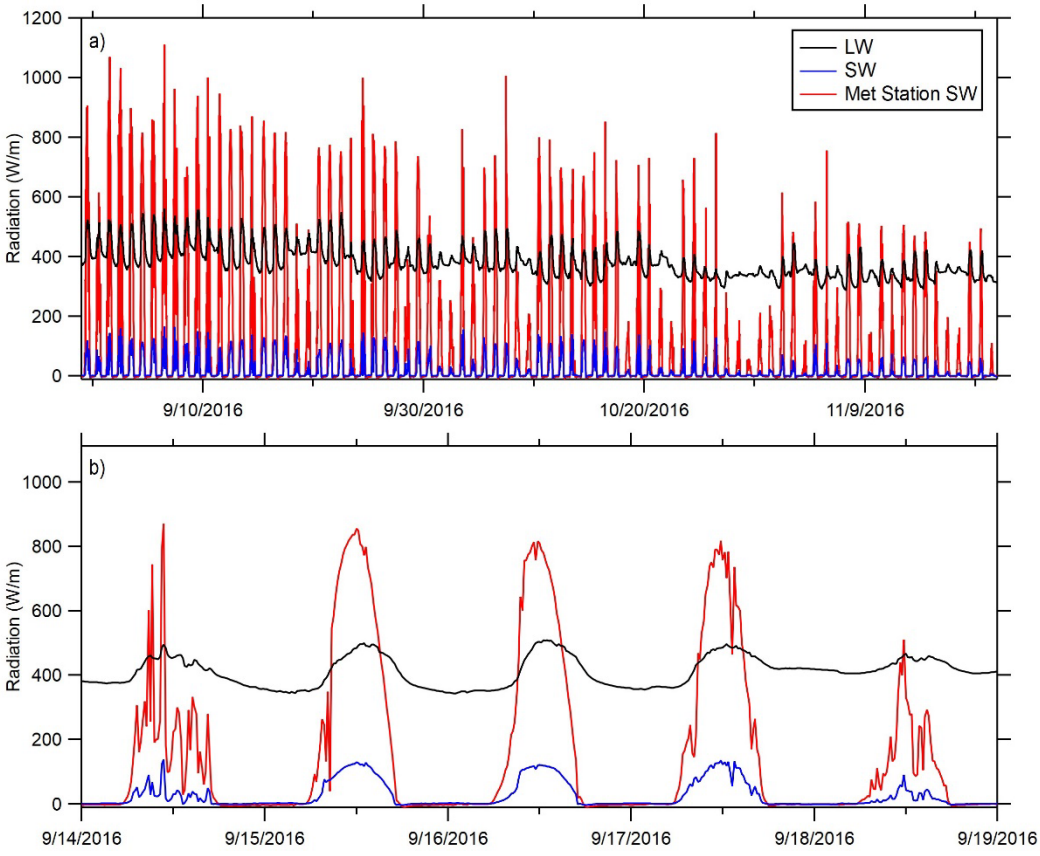

In addition to measuring incoming and outgoing solar radiation, we measured the surface reflected heat (W/m²) with two heat flux sensors located on the east and west side of the test plot. As expected, the diurnal heat flux pattern was similar to the incoming solar radiation pattern (Figure 16). The heat fluxes on the east side of the plot are not significantly different from those on the west side of the plot.

Figure 16. Surface reflected heat flux (W/m²) at the east and west of the plot from 30 August 2016 to 21 November 2016.

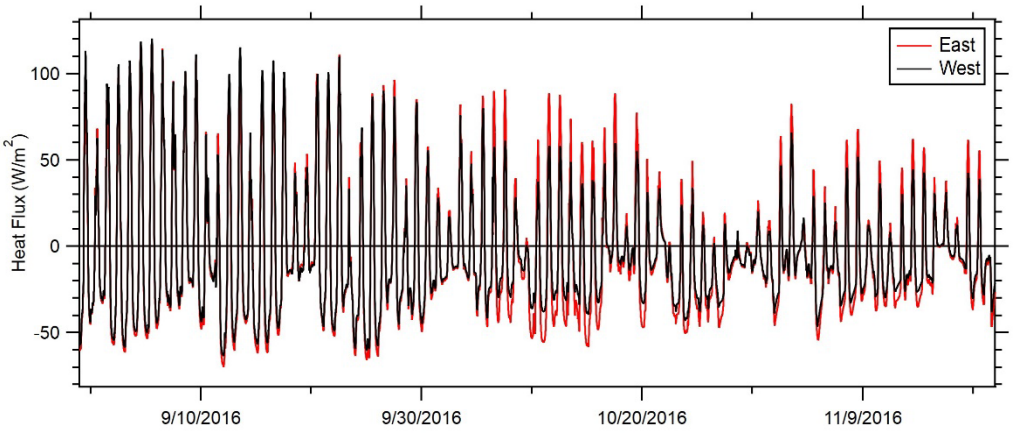

3.4 Soil properties

3.4.1 Grain-size distribution of soils

The soils at the test plots varied from a silty sand to silty clay. The northern portion of the test plot contained some gravel (Table 1). Overall, the grain-size spatial distribution was fairly homogeneous at the ground surface and at depth. Grain size did not appreciably change with depth down to 66 cm bgs.

Table 1. Grain-size distribution of soils.

Grid	Location and Sensor Type	Depth (cm)	Soil Description	Soil Type	% Gravel		% Sand			% Fines	
B13	at Center CS655	20.3–25.4	Silty Clay	CL	0	0	6	0	1	14	79
B13	at Center CS655	30.5–38.1	Silty Clay	CL	0	0	5	1	0	10	84
B13	at Center CS655	50.8–61.0	Silty Clay	CL	0	0	6	0	1	13	80
B21	at North CS616	0–7.6	Silty Sand	SM	0	7	5	35	35	10	8
B21	at North CS616	10.2–15.2	Poorly Graded Sand with Silt	SP-SM	0	5	3	55	27	6	4
B21	at North CS616	15.2–20.3	Silty Sand	SM	0	8	4	32	27	21	8
B21	at North CS616	20.3–25.4	Silty Sand	SM	0	11	4	27	28	22	8
B21	at North CS616	30.5–35.6	Silty Sand	SM	0	8	2	13	29	36	12
B21	at North CS616	45.7–50.8	Silty Sand	SM	0	6	3	17	46	19	9
B21	at North CS616	61–66.0	Silty Sand	SM	0	4	1	19	60	9	7

CL = lean clay, SM = silty sand, and SP-SM = poorly graded sand with silt.

3.4.2 Soil density

We measured the dry soil density with the eGauge at several grid locations (B1, B7, B9, B17, and B19) and depths (5.1, 10.2, 15.2, and 20.3 cm bgs). The density ranged from approximately 1525 to 1825 kg/m^3 (Figure 17) and increased with depth. The lowest soil dry density was in the north-western corner (B1). The variation in the dry soil density at the ground surface was more than 10%.

Figure 17. Soil density versus depth.

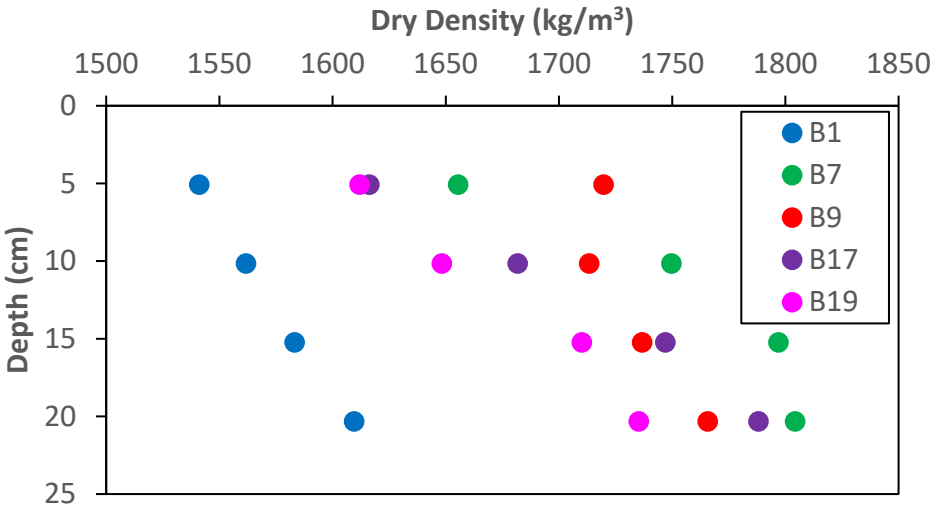

3.4.3 Soil chemistry

The metals Ag, Cr, Ni, Mo, and Sb were not detected in the soil with the XRF, but several other metals were detected (Table 2). The coefficient of variation (CV*) ranged from 12% (Fe, Mn, and Ti) to 87% (Cu). The spatial distribution of Mn and other metals exhibited a heterogeneous pattern (not shown). However, no relationship was apparent between specific metals in the soil and soil surface temperatures.

* Coefficient of variation is a measure of relative variability: CV = (standard deviation / mean)*100.

Table 2. Soil metal content (ppm) as measured by XRF.

Element	As	Co	Cu	Fe	Mn	Pb	Ti	Zn
Minimum	0	130	0	21,661	444	13	2848	41
Maximum	10	359	28	34,464	710	24	4342	72
Mean	6	223	13	26,110	537	18	3441	52
Median	7	208	18	25,913	522	18	3427	53
Standard Deviation	2	51	12	3059	65	3	421	8
Variance	5	2631	136	9×10^6	4217	9	2×10^5	61
CV	36	23	87	12	12	17	12	15

3.4.4 Volumetric water content of soil

At the center of the test plot, the predisturbance volumetric water content at a depth of 5.1 cm to 61 cm varied from 31% to 48% during September through November 2016 (Figure 18). Diurnal fluctuations in volumetric water content related to evapotranspiration is evident as are rapid increases in response to precipitation events. Surface-soil moisture has the greatest variance with the amount of variability decreasing with increasing depth. As with the soil temperature, there is a lag between soil moisture at the surface and at depth, which is related to the soil hydraulic conductivity. Lower soil moisture levels are apparent on the northern side of the test plot and higher to the south (not shown). This is consistent with the soil grain-size distribution, which exhibits higher clay content on the southern side of the test plot.

Figure 18. Volumetric water content of soil (%) by depth (5.1, 15.2, 30.5, 45.7, and 61 cm) at the center of the test plot.

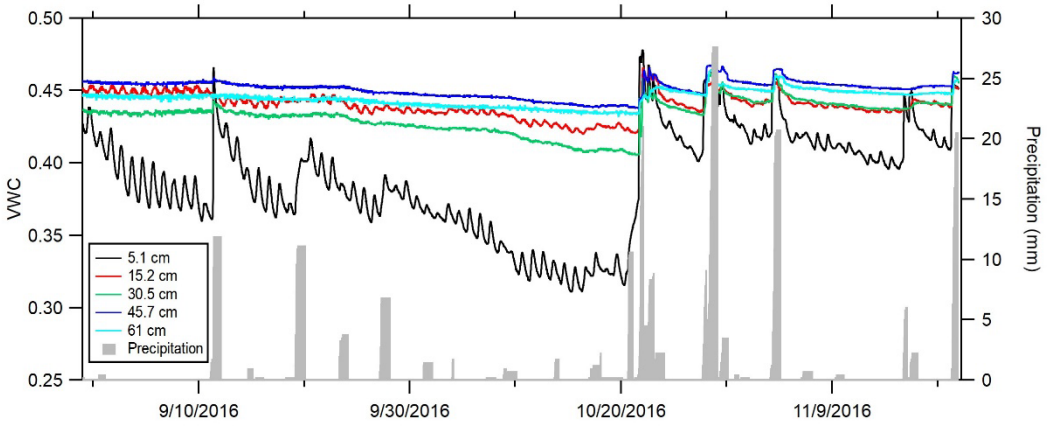

3.4.5 Bulk electrical conductivity

Changes in soil electrical conductivity with time and depth for the period of interest are similar to those for volumetric soil content where diurnal effects are also evident (Figure 19). The near-surface soil (5.1 cm bgs) at one of the center locations had the lowest electrical conductivity (about 0.14 dS/m) while at depth (15.2–61 cm bgs) the electrical conductivity behaves similarly with a small increase from 20.5 to 61 cm bgs. We found no relationship between soil electrical conductivity and the surface temperature. Although at the time of a precipitation event on 11 September 2016 (Figure 19), the electrical conductivity closest to the surface increased from about 0.25 to 0.6 dS/m. Similar increases occurred at all precipitation events (Figure 19).

Figure 19. Soil bulk electrical conductivity (dS/m) by depth (5.1, 15.2, 30.5, 45.7, and 61 cm) at the center of the test plot.

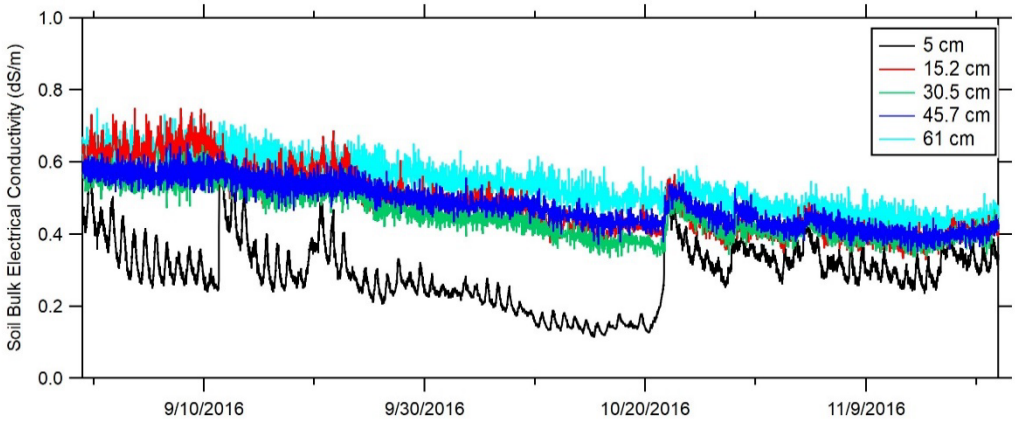

3.4.6 Soil temperatures

Figure 20 represents the temporal distribution of surface-soil temperatures at the test plot. Overall, surface-soil temperature decreases are consistent with seasonal trends. The lowest surface temperature during this period was −0.6°C measured on 27 October 2016. The diurnal temperature variability within the plot was negligible at 45.7 cm bgs and lower (results not shown). The diurnal variation is visible at 30 cm during all periods except immediately following the large rain event. The maximum distance between any pair of thermocouples in the test plot was less than 3.05 m.

The temperature fluctuations with depth in the center of the test plot indicate that variability decreases with increasing depth (Figure 20). Also visible in this plot is the lag between changes in surface temperature and

those at depth due to thermal inertia. Additionally, an overall seasonal decline in soil temperature as well as daily variability with the onset of winter is apparent.

Figure 20. Soil temperatures (°C) of (*a*) surface soil (0 cm bgs) measured at five locations (north [BNT], east [BET], center [BCT], south [BST], and west [BWT]) in the test plot and (*b*) soil temperature by depth (0, 5.1, 15.2, 30.5, 45.7, and 61 cm) at the BCT location.

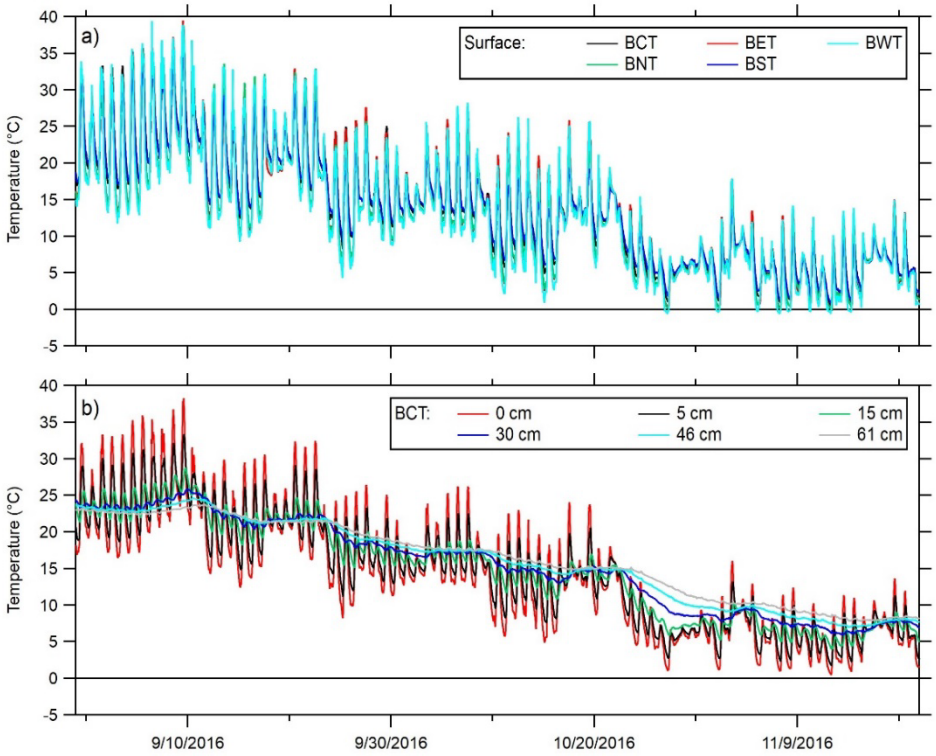

Figure 21 shows the spatial variability of surface-soil temperatures as measured from the IR images for 25 and 27 September 2016 at 1700 hours. Overall the surface-soil temperatures were lower on the 25th than the 27th but exhibited greater variability (Figure 21*b*). The sun angle at this time was 8°, corresponding to low incoming shortwave and longwave radiation forcing.

Figure 21. Surface-soil thermal variability (°C) as measured with the IR camera for (*a*) 25 and (*b*) 27 September 2016 at 1700. (*c*) Surface-soil temperature measurements from BCT, BWT, BST, BET, and BNT.

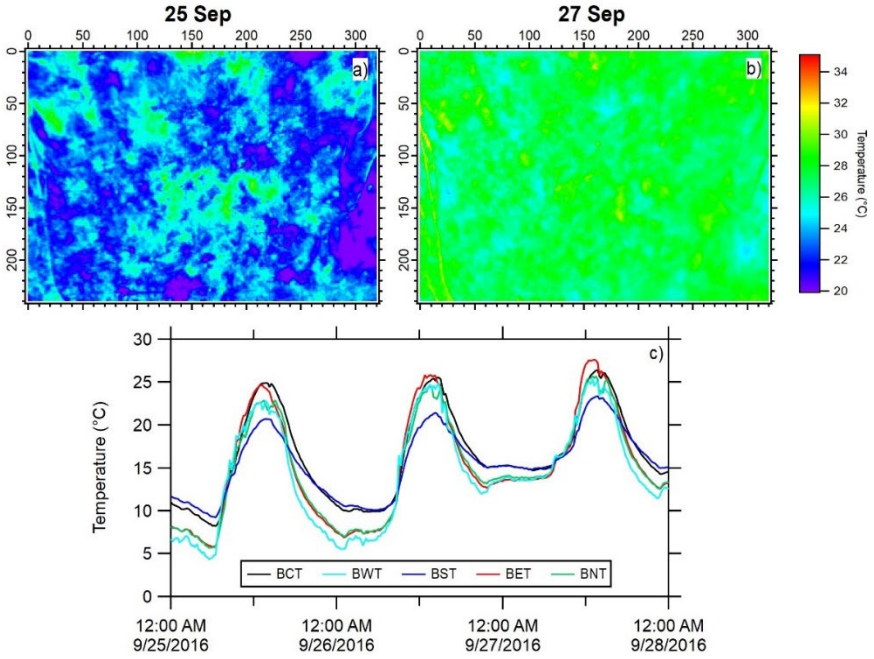

3.5 Thermal Response Variance to Weather Events and Temporal Changes

Figure 22*a–f* compares surface thermal images before any objects were placed. These images were taken at the time of maximum air temperature (a–c) and at 1700 (d–f) on three consecutive days in September and show the IR sensitivity to weather conditions. The maximum air temperature was 15.92°C (at 1400), 18.84°C (at 1445), and 22.44°C (at 1615) on 25, 26, and 27 September, respectively (Figure 22*g*). On 27 September, a precipitation event started early in the morning at 0105 and ended at 0500 after a cumulative amount of about 7 mm. The lowest relative humidity occurred on 25 September (Figure 22*h*), and the wind velocity varied over these three days with a maximum of 3.1 m/s on 25 September (Figure 22*i*). There is a noticeable contrast across the test plot on all days despite similar air temperatures and wind speeds when the images were taken. Similar patterns are discernable between the 26th and 27th.

Figure 22. Comparison of IR camera images taken in the early afternoon for (*a*) 25 September, (*b*) 26 September, and (*c*) 27 September and (*d–f*) the late afternoon. The corresponding figures for (*g*) air temperature and cumulative 24 hr precipitation (Precip), (*h*) relative humidity (RH), and (*i*) wind velocity are provided below the IR images.

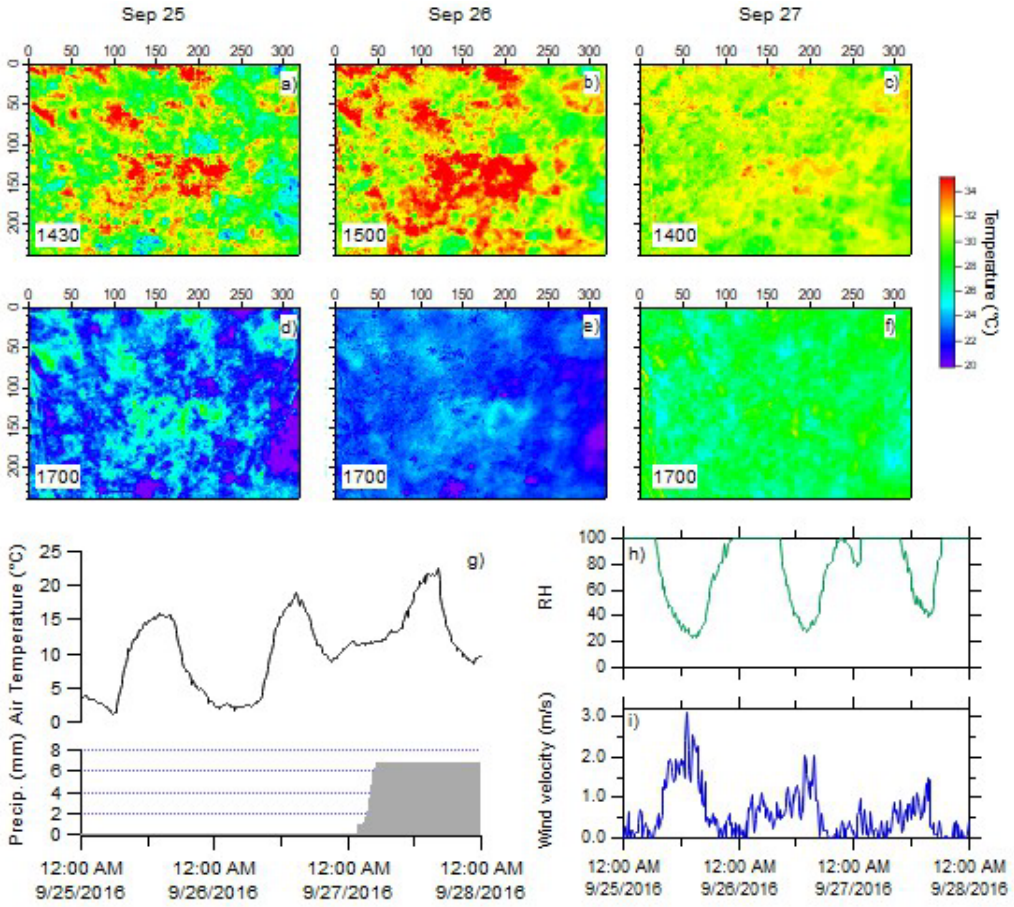

By fitting theoretical variogram models to empirical semivariograms, the spatial relationship with parameter estimates can be quantified (see section 2.8). The parameter estimates are then used to represent individual plot spatial variations, allowing comparisons between different times and conditions. This enables statistical testing by controlling the external forcing parameters. Quantifying the external variables will help inform us on what controls both the differences and similarities in the spatial structure of the soil plot. Figure 23 shows variograms of the images from 25 to 27 September (Figure 22). Looking at the contour plots in Figure 21, it would appear that the maximum variance occurs on 25 September at 1430. However, the variogram in Figure 23 indicates that the maximum variance actually occurs at 1700 on 25 September.

Figure 23. Variograms for 25–27 September 2016 corresponding to the thermal images in Fig. 22. The unit of lag (*h*) is millimeters.

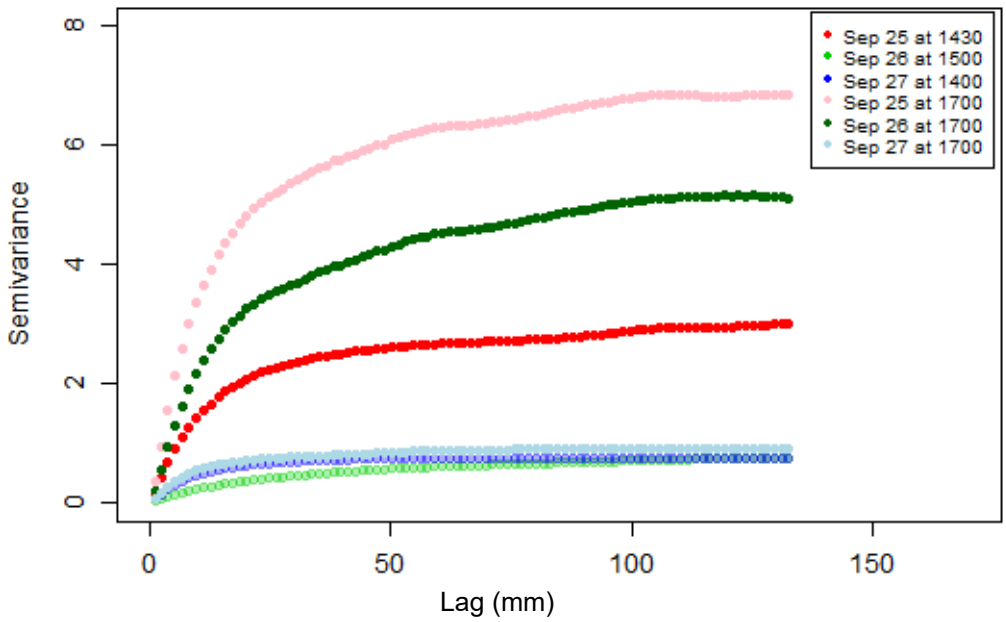

Using the results from 25–27 September, the first external variable studied was weather forcing. This study considered three different weather conditions: "fair," "cloudy," and "rain." The cloudy category was defined as every day that was not completely clear or completely rainy. Thus, days that had weather reports of "scattered clouds," "partly cloudy," "overcast," "fog," and "cloudy" were placed in the cloudy category. The data were log transformed due to a lack of normality and the presence of heteroscedasticity (variability is not evenly distributed).

Tables 3 and 4 provide the results from the one-way ANOVA and Tukey HSD test for the three weather conditions. These results and the log-transformed boxplots of the variograms (Figure 24) reinforce the variograms illustrated in Figure 25. Analysis from these 3 days indicate that the different structures of the variograms are affected and determined by the weather condition. To further test this, we calculated the spatial variograms of the surface thermal response for 23 days, characterizing each weather condition (Figure 25). The thermal variance is greatest on fair days and decreases with increasing cloud cover. Periods of rain and soil saturation result in the smallest thermal variance. In other words, soil surface thermography is correlated at further distances during rain events. The lack of spatial variability in surface-soil temperature during rain events means that abnormal deviations due to subsurface objects can potentially be more easily identified when the soil is wet. However, we found

that the buried objects were not detectable following rain events (lag time varies by precipitation intensity and duration). This is due to the movement of rain, which has a uniform temperature, through the soil decreasing the soil temperature variability.

Table 3. One-way ANOVA of variogram sill estimates by weather event.

Group	Degrees of Freedom	Sum of Squares	Mean of Squares[a]	*F*[b]	*p*-Value
Weather Event	2	31.24	15.62	19.77	2.23×10^{-5}
Error	19	14.96	0.79	–	–

[a] Mean of squares = sum of squares / degrees of freedom

[b] *F* = sum of squares / mean of squares

Table 4. Tukey HSD by group analysis of meteorological conditions.

Group	Difference	Lower Bound	Upper Bound	*p* Adjusted
Fair–Cloudy	1.35	0.22	2.49	0.0181
Rain–Cloudy	−1.58	−2.84	−0.33	0.0122
Rain–Fair	−2.94	−4.13	−1.75	<0.001

Figure 24. Log-transformed boxplots of the variogram sills by weather event for cloudy, fair, and rain conditions.

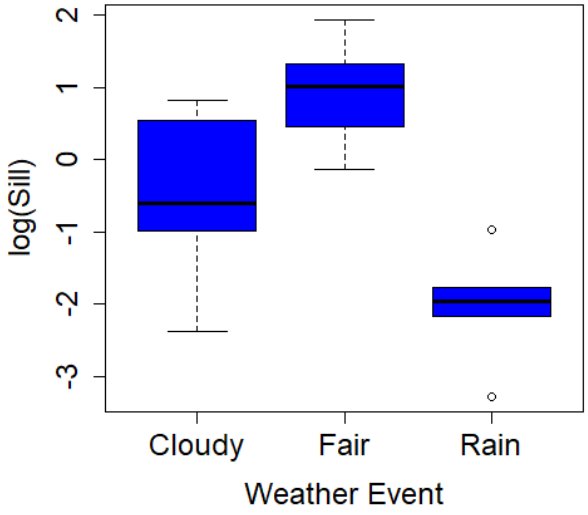

Figure 25. Semivariograms for 23 days of specific weather events: fair, cloudy, and rain. The semivariograms are constructed from thermal images at 1000 hr for each day.

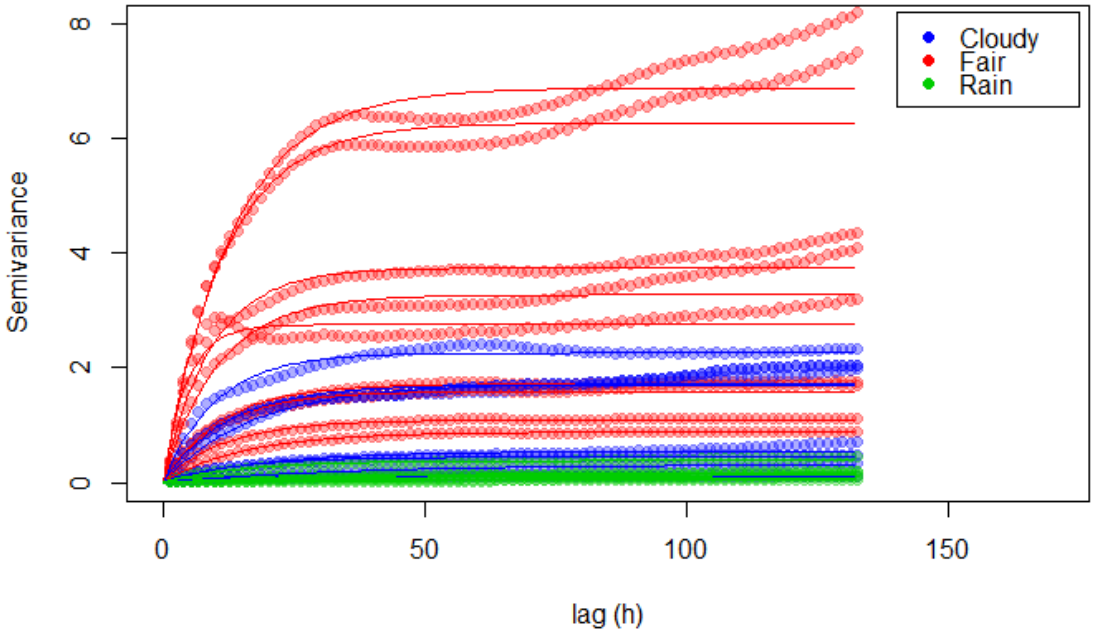

In addition to investigating the variance of multiple days for different weather events, we also looked at the hourly variance. Figure 26 shows the semivariograms on 7 November 2016 from 0000 to 2300, one month after the objects were emplaced. The air temperature varied from about −4°C at night to about 11°C at 1600. There was light rain (0.8 mm) during the early morning on 6 November 2016. The periods of rain resulted in lower semivariance values and sills occurring earlier than for fair conditions. It is interesting to note that the range is approximately the same as the cross-sectional object length.

Figure 26. For 7 November 2016, (*a*) variograms for each hour and (*b*) air temperature.

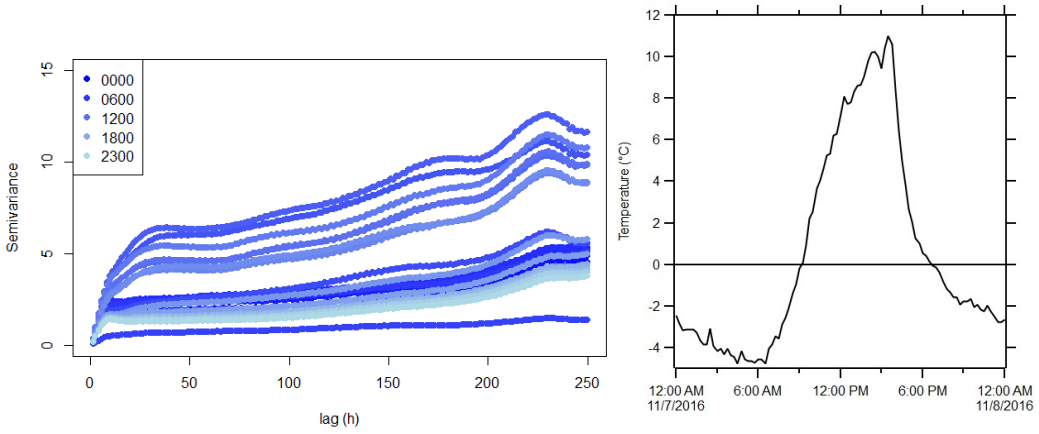

3.6 Thermal Response and Heat Flux Investigations

3.6.1 Soil temperature response as indicated by IR imagery

To understand how buried objects affect the thermal response, we compared the thermal images from buried objects (see Rectangular Plastic, Round Plastic, Rectangular Metal, and Round Metal in Figure 4) to close-by areas where no objects were buried (see Control 1, 2, 3, and 5 in Figure 4). Figure 27 depicts the normalized surface-soil temperature as measured with the IR camera for 20 September to 20 October 2016. This period spans before and after object emplacement, which occurred on 7 October. Diurnal fluctuations in surface-soil temperature are evident before object emplacement with changes in the ±2°C range for the disturbed cells. However, after object emplacement, there is a clear increase in thermal response of ±6°C. The magnitude of the thermal response varies by the size and material type of the object buried.

Figure 27. Normalized surface-soil temperature for select cells within the plot as measured with IR.

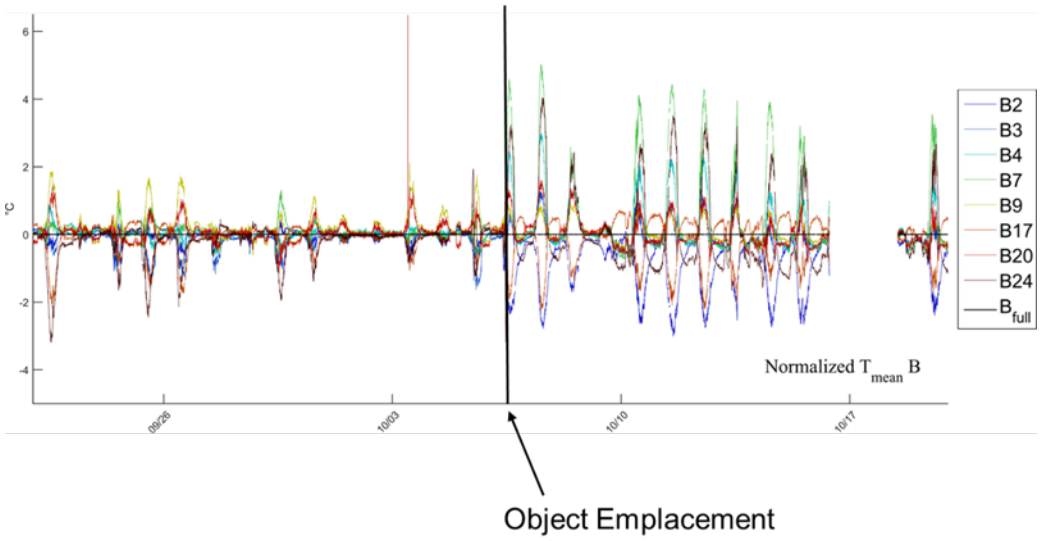

We analyzed the 25 September (before emplacement), 9 October, and 7 November (both after emplacement) more closely. Figure 28 shows the averaged soil temperature every 15 minutes (96 comparisons for each day) as measured by IR for each object and control area. The before-emplacement comparison is identical for three of four objects. For the Rectangular Plastic object, there is some discrepancy between Control 1 and the object (Figure 28*a*). We also see this for the Round Plastic and Control 2; but if we look at the difference between that object and Control 5, the temperature

is almost the same (Figure 28*b*). Only one object, the Round Metal, shows no difference between the object and control. We believe this result is due to the Round Metal object having 1/10 the mass and size of the other three objects. For the other three objects, the soil temperature above the object is lower than the control in the early morning, evening, and night. The greatest difference in soil temperatures above the object and its control is observed early evening/night. On 7 November the opposite is true: during midday, the temperature at the object is greater than the temperature at the control.

Figure 28. Soil temperatures at buried-object areas compared to control areas for 27 September (before emplacement), 9 October, and 7 November.

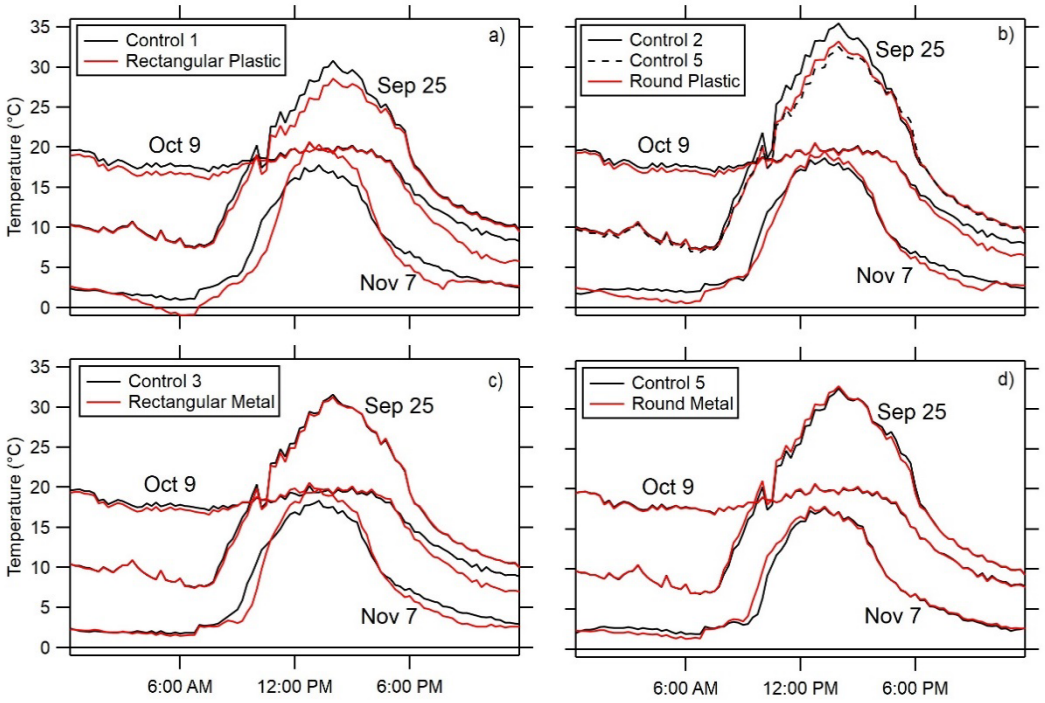

3.6.2 Heat flux

The following questions arise when making observations of IR-image data collected from a plot where objects are known to be buried: What information is here? What are we really seeing? What does it mean? Additionally, can knowledge of the soil plus IR images inform what we are seeing and why?

Changes in IR images with time at a given location contain a wealth of information. To demonstrate this, we chose two after-emplacement images: 0000 and 1200 on 9 October 2016 (Figure 29*a* and *b*). The temperature

range of both images is 16.5°C–20.3°C. The square object on the left side of both images is the white plate used to calibrate the IR camera on the plot surface. Differential heating between the sample times can be observed by subtracting the two images (dotted lines Figure 29*c* and *d*). These lines confirm what is seen visually, that there is a greater temperature change over the white plate than the buried object during this time period and that the greatest differences occur at the plate and object boundaries.

Figure 29. IR camera images taken on 9 October 2016: (*a*) 0000, (*b*) 1200, (*c*) temperature difference across line 1, and (*d*) temperature difference across line 2. *Red* = 0000, *Blue* = 1200; *solid* = ∇T, *dashed* = $\nabla^2 T$, and *black dotted* ΔT = (1200–0000).

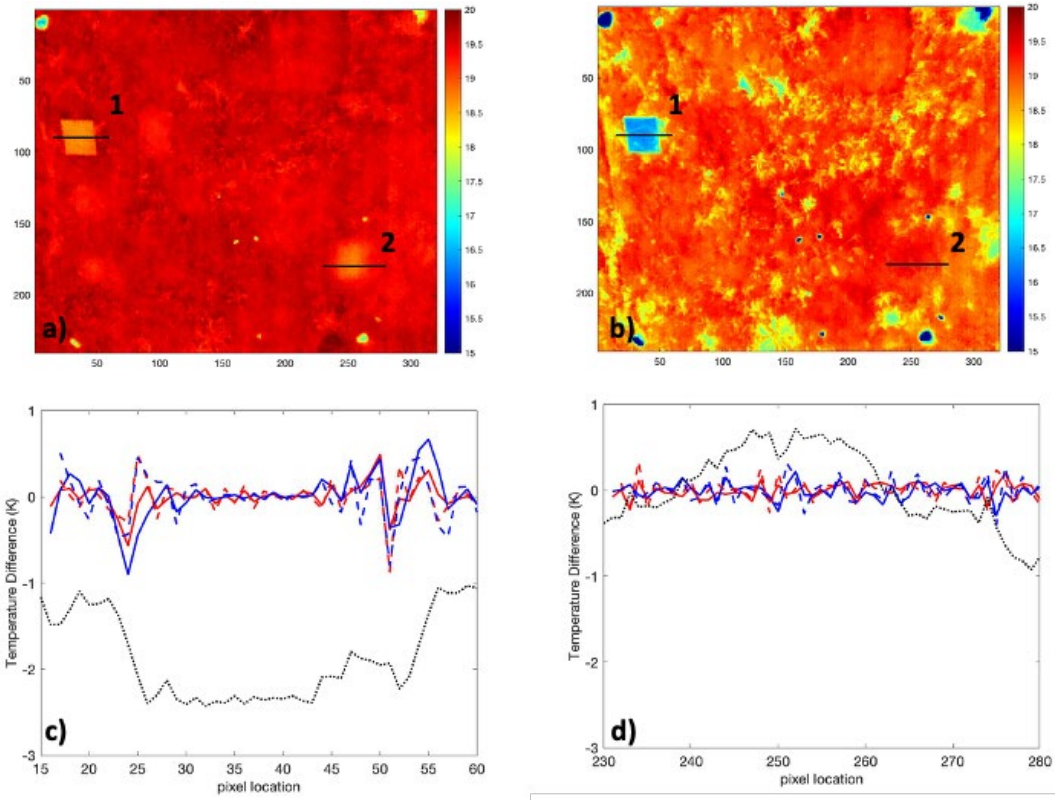

Also plotted in Figure 29*c* and *d* is the temperature gradient (∇T) along the profile lines shown in Figure 29*a* and *b* as a function of pixel-to-pixel distance (solid lines) as well as the spatial derivative of the gradient ($\nabla^2 T$, dashed lines) along the profiles. The greatest differences are found at the edge of the plate along line 1. Fourier's law of heat conduction gives

$$q = -\mathrm{k}\nabla T, \tag{4}$$

where

q = the heat flow (W/m²),
k = the thermal conductivity (W/m·K), and
∇T = temperature change (K/m).

The change in stored energy in a volume of soil, assuming that there is no internal energy source, is

$$\frac{\partial Q}{\partial t} = c_p \rho \frac{\partial T}{\partial t}, \quad \Delta Q = c_p \rho \Delta T, \tag{5}$$

where

Q = stored energy (J/m³),
c_p = specific heat (J/kg·K), and
ρ = density (kg/m³).

Conservation of energy dictates that the change in stored energy is

$$\Delta Q = -\nabla q, \quad \rho c_p \Delta T = -\nabla(-k \nabla T) = k \nabla^2 T, \quad \Delta T = \alpha \nabla^2 T, \tag{6}$$

where α is the thermal diffusivity (m²/s, $\alpha = k/\rho c_p$), which represents the thermal inertia of a substance. Equation (6) assumes that the thermal properties of the soil are uniform. The thermal properties and density of soils is a function of the portion of minerals, organics, air, water vapor, ice, and liquid water present (Farouki 1981; Johansen 1975).

Contour plots of ΔT can be constructed for the entire test plot where each contour line reflects a defined magnitude of change and the space between the contour intervals represents the flux gradient (Figure 30). Regions with large changes inform which areas to target for further examination.

To see if additional information could be extracted from the images, $\Delta T - \Delta T_{mean}$ was investigated in addition to ΔT. Figure 31 shows the results for $\Delta T - \Delta T_{mean}$ on 9 October between 0000 and 1200. Comparing Figure 30*b* and Figure 31 shows that some of the background clutter is smoothed and that areas of greater relative change become highlighted, but not to an extent to further pursue this method.

Since temperature changes with distance and not just time, as indicated in equation (4), we calculated ∇T along four horizontal transects at 90, 180, 190, and 220 pixel levels (see Figure 29*c* for reference) for 0000 and 1200 on 9 October 2016. Also plotted in this figure is the thermal temperature (T) along the horizontal transect. From this figure, it is difficult to extract the location of any object whether on the surface or buried when using ∇T except perhaps at the object edges as was noted previously. If instead the thermal temperature profile along the transects is studied, both of the Plastic objects along the 90 pixel transect (see Figure 4) are easily discernable and are colder than the surrounding soil (large dip in blue curves). The Plastic objects are also detectable on the 180 transect at 0000. For both of these times, the metal objects are not findable. Clearly, this method is not optimal for finding emplaced objects and is worse than a simple temperature profile.

Figure 30. Change in temperature between 0000 and 1200 on 9 October 2016 where darker red indicates more positive change in temperature and blue shows a negative change. (*a*) 1.0 °C contour intervals, (*b*) 0.5 °C contour intervals, and (*c*) three-dimensional combined surface and contour plot using 1.0 °C intervals.

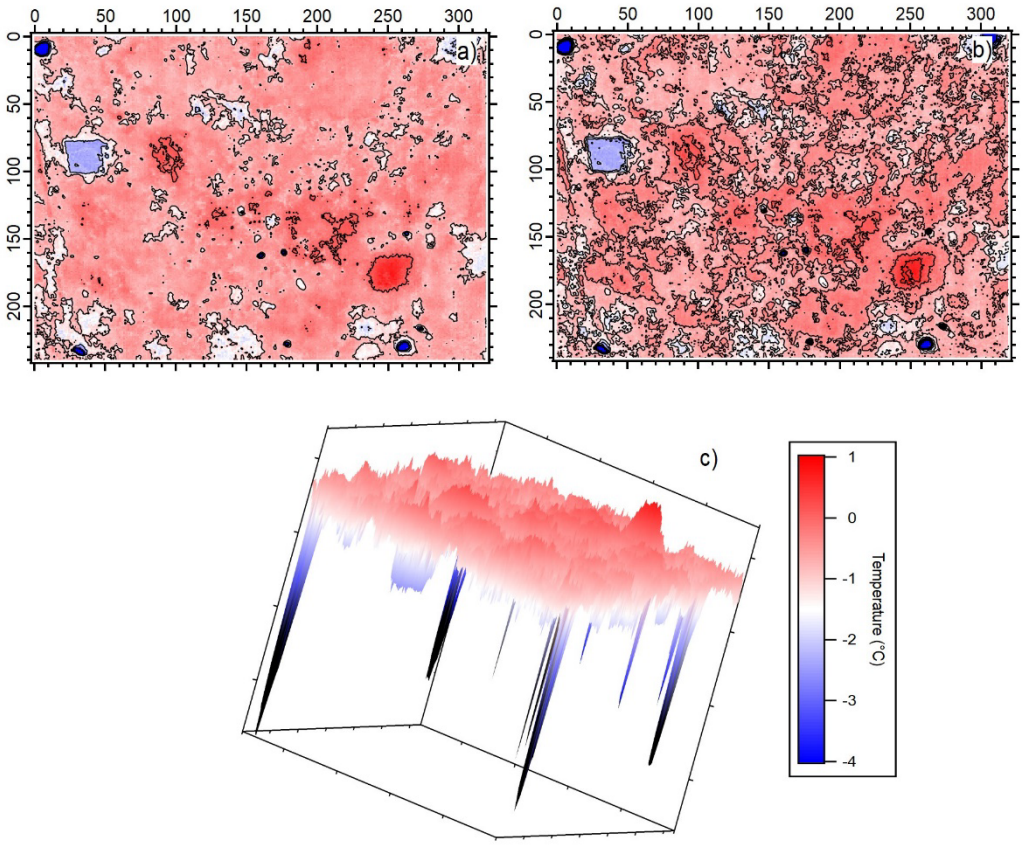

Figure 31. Contour plot of $\Delta T - \Delta T_{mean}$ between 0000 and 1200 on 9 October 2016. The contour interval is 0.5 °C.

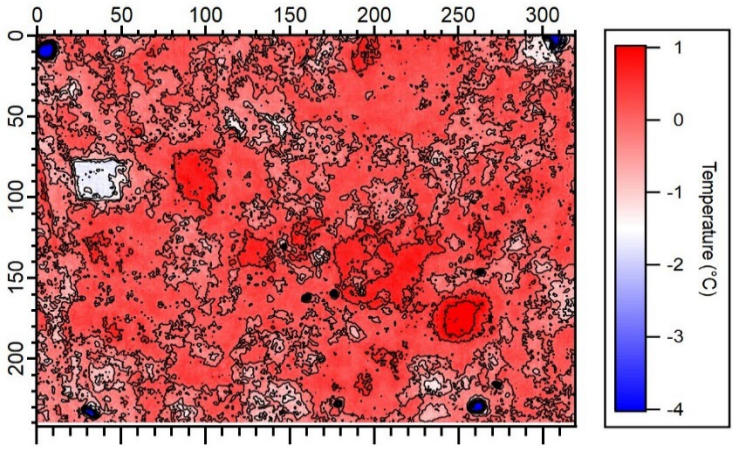

Figure 32. Plot of ∇T and actual T on 9 October 2016 at (*a*) 0000 and (*b*) 1200. *Solid* = ∇T, *dashed* = T; *blue* = 90, *black* = 180, *red* = 190, and *green* = 220.

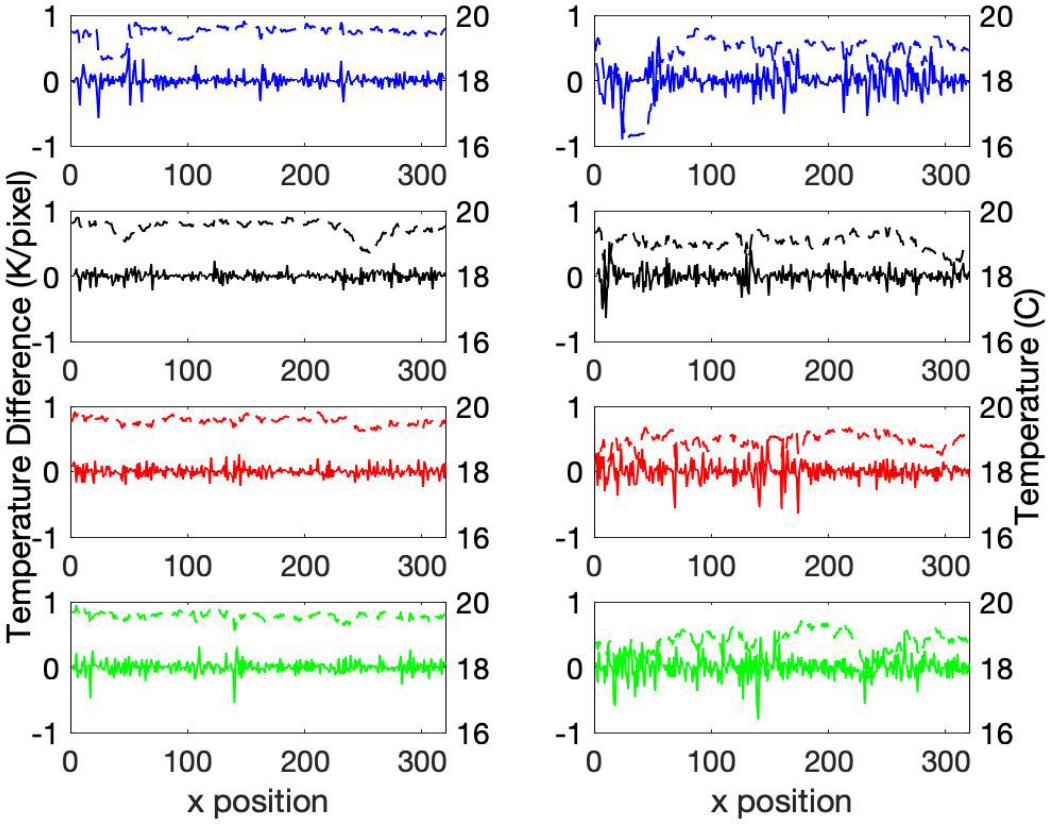

The result of $\Delta T - \nabla^2 T$ was assessed with the site data, ignoring thermal diffusivity effects. Figure 33 shows the results for the two images of interest. Greater contrast is revealed in distinct areas of the image compared to the other methods considered. Areas highlighted in the 0.5 band (light blue in Figure 33*a* and light green in Figure 33*b*) show regions of least change and possible areas of further interest.

Figure 33. Contour plot of $\Delta T - \nabla^2 T$ between 0000 and 1200 on 9 October 2016 (*a*) using a 1.0 °C contour interval and (*b*) using a 0.5 °C contour interval.

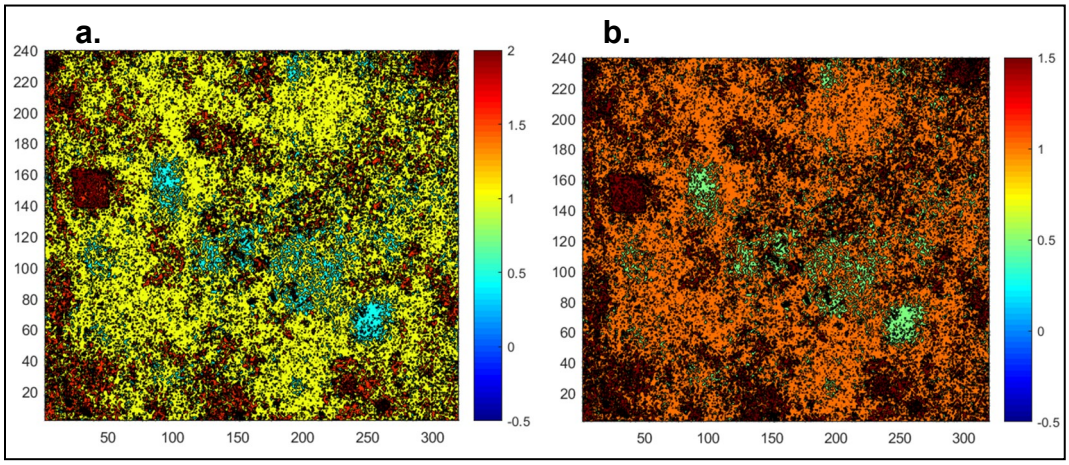

The preceding analyses have shown that by examining changes in temperature temporally and in combination with spatial changes, areas of interest can be identified even in the absence of material property information or knowledge of the system history. The previous investigations used two randomly chosen points. Further information may be obtained by systematically choosing instances when the average ΔT is greatest.

Figure 34 and Figure 35 show how ΔT changes over the course of 2 days where, in this instance, $\Delta T = T_i - T_{0000}$ and T_i is the temperature at 15-minute intervals starting at 0000 and ending at 2400.

On both days, ΔT_{min} occurred at 2400. On 9 October 2016, ΔT_{max} happened at 1230; on 23 October 2016, it was at 1400. Also shown on these plots is the standard deviation of the temperature, essentially the normalized values, at 0000, ΔT_{max}, and ΔT_{min} as well as the difference between them (ΔT_{max} – 0000, $\Delta T_{max} - \Delta T_{min}$, and $\Delta T_{min} - T_{0000}$). On both days, the white calibration plate and buried rectangular objects are most visible at 0000 and 2400. On 9 October 2016, all of the buried objects, except the Round Metal object, are easily discernable in both the $T_{1230} - T_{0000}$ and

$T_{2400} - T_{1230}$ images. On 23 October, the metal objects are harder to see when looking at $\Delta T_{max} - T_{0000}$ and $\Delta T_{max} - \Delta T_{min}$. This analysis shows that objects become most visible during periods when there is a rapid negative change in temperature.

Figure 34. Average temperature differences between 9 October 2016 at 0000 to 10 October at 0000 (*red line*) on 15-minute intervals with selected thermal IR images (*green* color scheme) and calculated temperature difference (*brown* color scheme).

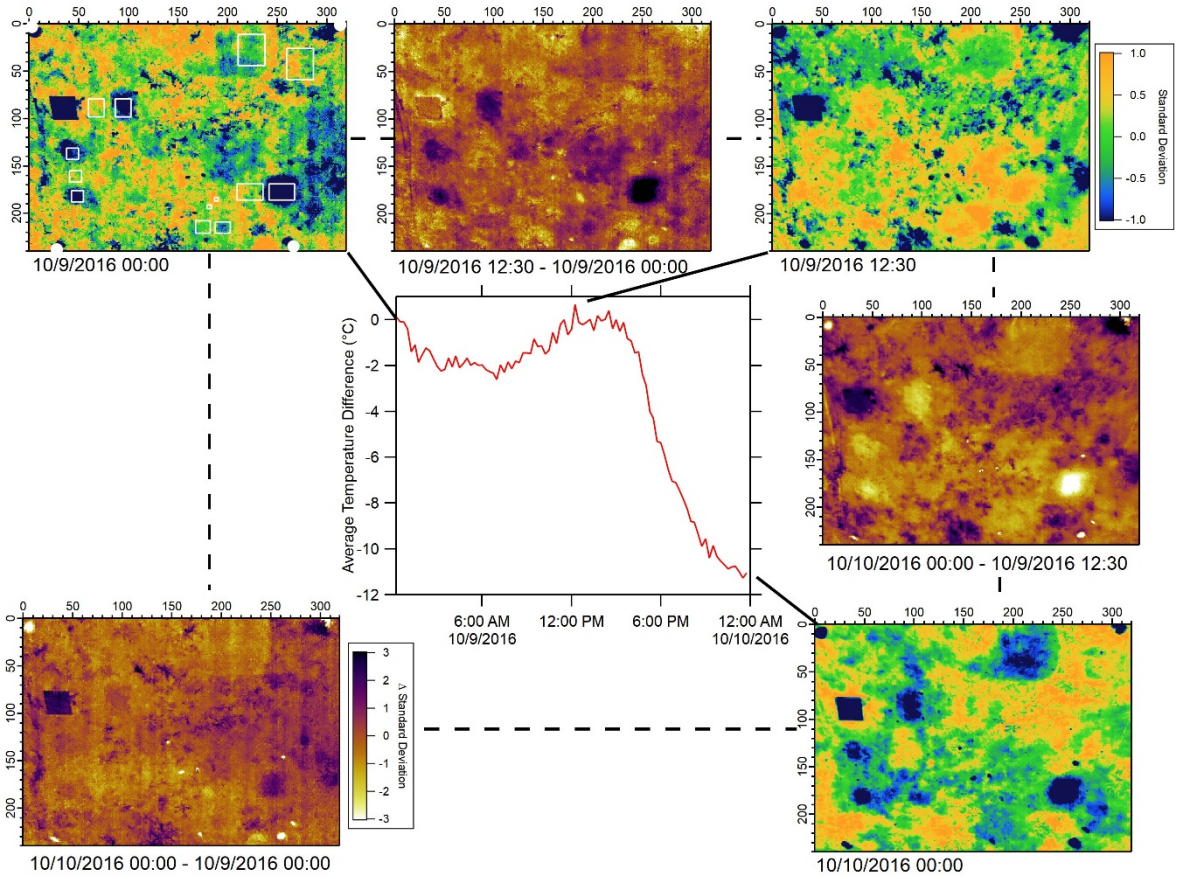

Figure 35. Average temperature differences between 23 October at 0000 and 24 October at 0000 (*red line*) on 15-minute intervals with selected thermal IR images (*green* color scheme) and calculated temperature difference (*brown* color scheme).

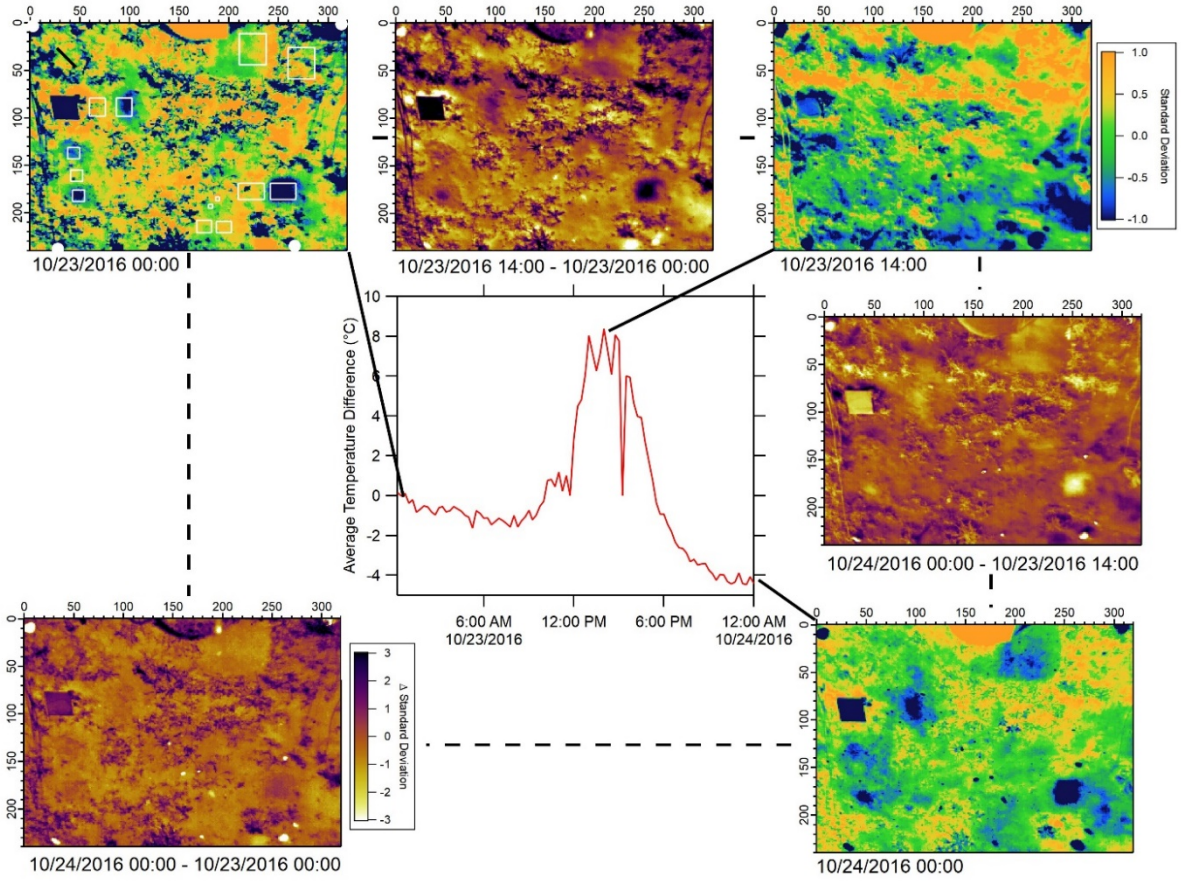

3.6.3 Limitations

Several sensors for heat flux, soil moisture, and temperature were installed in the plot at varying depths (Z) and spatially distributed (X–Y) within the plot (section 2.6). One of the limitations to using the sensor data to calculate the heat flux (equation [6]) is the small number of sensors within the plot. This results in sparse coverage of the plot with respect to its size. By creating a representative grid of the plot and placing the recorded data points therein, the gaps in coverage become obvious. Considering the relative position and distance between each sensor helps to avoid overly simplifying assumptions as to the heterogeneity of the plot. Without interpolating between the sampled regions, our understanding of the system as a whole is limited.

The above discussion is illustrated using the thermocouple-measured surface temperatures. The thermocouples are located at grids B3, B13, B15,

B21, and B23 (Figure 3, Figure 36*a*). To populate the remaining grids, we used a manual averaging method. A minimum of three surrounding grids needed to be filled before the average was calculated. Our grid-filling order was subject to user discretion and resulted in as much as a 1.0°C difference in final temperatures (not shown). To generate the results shown in Figure 36*b*, at each step the empty cell with the greatest number of filled neighbors was chosen. In the case where two cells had the same number of adjoining filled grids, if one of those was a measured value, that cell was filled first.

Further interpolating the data beyond the plot 5 × 5 array to that of the IR images (240 × 320) used the MATLAB *interp2* function (Figure 36*c*). A similar technique can be used for any other measured property.

Figure 36. A schematic showing the process of interpolating a small number of temperature (Kelvins) data points across the plot over the entire area using a multistep method: (*a*) initial array (dark blue values are areas with no data), (*b*) interpolation of missing values using nearest neighbor averaging, and (*c*) final scaling to the thermal IR grid using cubic interpolation.

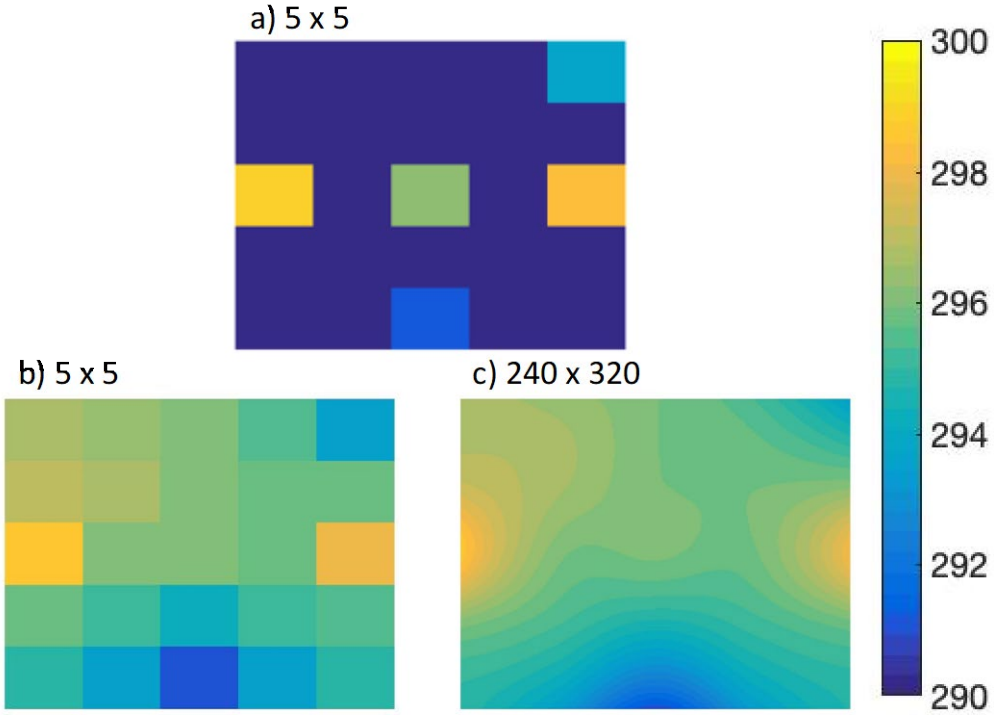

4 Conclusions

The thermal response for the buried objects varied by the size, mass, and material. We believe this response is due to changes in soil thermal properties caused by increased porosity (bulking) of the disturbed soil and not so much the objects themselves. This is based on the observation that the disturbed location without a buried object was visible at similar times as the locations with buried objects. Although, the buried-object temperature difference was larger than for the disturbed non-object location, except for the small Round Metal object. Contrary, to earlier work, this change in thermal response is persistent at the CRREL test over the 4 month duration despite multiple precipitation events (i.e. the thermal signature did not fade with time).

Thermal response for the Rectangular Plastic object was more apparent than for the Round Plastic object. For the Rectangular Metal object, the response was similar to the plastic objects; but for the Round Metal object, there is was no visible response. The lack of thermal response from the small Round Metal object is likely a function of the lesser amount of disturbed soil and the thermal mass being insufficient to manifest a significant differential temperature response as compared to the surrounding soil. Initial qualitative analysis suggests that surface thermal spatial patterns are a function of incoming solar radiation, air temperature, subsurface-soil temperatures, and moisture content.

During periods of solar input, the surface soil located directly above a buried object heats more rapidly than the surrounding soil, creating a temperature differential as compared to the surrounding undisturbed soil. Although some of this difference is due to physical disturbance of the soil where the object is emplaced, there appears to be an additive effect due to the object itself. It seems that the size, mass, and material of the buried object affect both the thermal capacity and the rate of thermal loading. For example, locations with buried plastic objects have higher surface-soil temperatures as compared to the buried Rectangular Metal object. Initially, the plastic material absorbs thermal energy more quickly than metal objects, resulting in greater temperature differentials with the surrounding soil. Metal objects have a higher thermal inertia than plastic objects. This contrast results in improved visibility for a longer period of time for plastic versus metal buried objects. Conversely, plastic objects during an absence of solar thermal loading cool more rapidly than metal objects and cool

faster than the surrounding soil. Very small objects such as the small metal object have insufficient thermal capacity to create a temperature differential with the surrounding soil. In addition, small objects require less physical disturbance of soil. Consequently, small buried objects are more difficult to see due to the inability to differentiate the response from background noise.

One of the observations from viewing the spatial data is that the soil surface temperature is not constant throughout the study area at any given point in time. The surface-soil temperature is distributed heterogeneously (i.e., there are clusters of elevated and lower temperatures) with values varying as much 7°C across the test plot. This heterogeneous distribution of surface-soil temperatures was apparent prior to object emplacement and continued after object emplacement. Further complicating the situation is that the surface-soil temperature is not constant throughout a 24-hour cycle. The diurnal solar loading results in a peak and trough fluctuation in average soil temperature response each day across the entire plot. However, the temporal changes do not result in a consistent thermal loading within the test plot (i.e., the location of clusters of elevated and lower temperatures changes as does the magnitude of thermal response).

Consequently, comparing two different days with identically environmental conditions for a given time of day does not produce the same spatial thermal response. In some instances, the difference in average thermal response can be explained by changes in air temperature, changes in solar input due to cloud cover, or precipitation events changing the soil moisture content. However, the heterogeneous distribution of soil temperature (i.e., clustering) appears unpredictable. This is not problematic for seeing larger buried objects; but for small objects with poor thermal conductivity and less soil disturbed, the thermal noise makes the objects invisible.

Although, we have been able to identify the general time of day with a high probability of object visibility for objects constructed of different materials, size, and shape, there are exceptions. We continue to pursue identification of the phenomena responsible for the variability in surface-soil temperatures at the scale of buried objects of interest.

In summary, the plot soil data can be extrapolated and interpolated to build a model of the system. We have yet to determine the fidelity of those extrapolations and interpolations as they relate to real data. We are unable

to predict how current and antecedent conditions combine to produce surface temperature distributions (without building a full-physics, high-fidelity model of the site). Also, it is unclear at present how far we can generalize our findings from the CRREL field location to a generally useful operations tool. With the large data sets collected at the CRREL test plot, it should be possible to generate relationships between the sensor data and the IR images to help understand the heat-flow energy transfer interplay between the atmosphere, surface soil, and buried objects. A model can be used to test these hypotheses through a sensitivity analysis and by comparing model synthetic scenes of the test plot with actual IR imagery and noting the similarity or differences. This is important to help understand the physical phenomena in play and ultimately to being able to explain this mathematically so that existing automatic target recognition software can incorporate this knowledge.

Before a model of the system can be developed, the remaining work needs to be completed: correcting images for keystoning, automating data aggregation and interpolation, generating a modeled three-dimensional volume of the plot to use as an artificial test plot, calculating the effects of weather and albedo on the surface temperature and heat flux, and determining the best way to account for foreign-object-driven anomalies.

In the end, the information gathered from this analysis should help to identify those variables influencing the thermal response of a buried object. By better understanding and quantifying the environmental processes affecting IR imagery, we hope to improve false alarm mitigation and improve our ability to detect and identify buried objects.

References

ASTM. 2007. *Standard Test Method for Particle-Size Analysis of Soils*. ASTM D422-63(2007)e2. West Conshohocken, PA: ASTM International.

Carson T., and C. Salvaggio. 2015. "Soil Signature Simulation in the Thermal Infrared." *Optical Engineering* 54:104102.

Chair, Z., and P. K. Varshney. 1986. "Optimal Data Fusion in Multiple Sensor Detection Systems." *IEEE Transactions on Aerospace and Electronic Systems* AES-22 (1): 98–101. https://doi.org/10.1109/TAES.1986.310699.

De Jong, W., and H. A. Lensen, and Y. H. L. Janssen. 1999. "Sophisticated Test Facility to Detect Land Mines." *Proceedings of SPIE* 3710:1409–1418.

Farouki, O. T.1981. *Thermal Properties of Soils*. Monograph 81-1. Hanover, NH: U.S. Army Cold Regions Research and Engineering Laboratory.

Hong, S., T. W. Miller, B. Borchers, and J. M. H. Hendrickx. 2002. Land Mine Detection in Bare Soils Using Thermal Infrared Sensors. 2002. In *Proceedings of SPIE 4742, Detection and Remediation Technologies for Mines and Minelike Targets VII*, 1–5 April, Orlando, FL. https://doi.org/10.1117/12.479124.

Johansen, O. 1975. "Thermal Conductivity of Soils." PhD thesis, Norwegian Technical University, Trondheim, Norway. CRREL Draft Translation 637, 1977. Hanover, NH: U.S. Army Cold Regions Research and Engineering Laboratory. https://apps.dtic.mil/dtic/tr/fulltext/u2/a044002.pdf.

Khanafer K., and K. Vafai. 2002. "Thermal Analysis of Buried Land Mines over a Diurnal Cycle." *IEEE Transactions on Geoscience and Remote Sensing* 40 (2): 461–473.

Khanafer K., K. Vafai, and B. A. Baertlein. 2003. "Effects of Thin Metal Outer Case and Top Air Gap on Thermal IR Images of Buried Antitank and Antipersonnel Land Mines." *IEEE Transactions on Geoscience and Remote Sensing* 41 (1): 123–135. https://doi.org/10.1109/TGRS.2002.807755.

Koenig. G., Y. Koh, S. Howington, and C. Scott. 2008. "Phenomenology of Thermal Signatures of Disturbed and Undisturbed Soils." In *Proceedings of SPIE 6953, Detection and Sensing of Mines, Explosive Objects, and Obscured Targets XIII*, 16–20 March, Orlando, FL. https://doi.org/10.1117/12.777790.

Kylili, A., P. A. Fokaides, P. Christou, and S. A. Kalogirou. 2014. "Infrared Thermography (IRT) Applications for Building Diagnostics: A Review." *Applied Energy* 134:531–549.

Moukalled, F., N. Ghaddar, H. Kabbani, N. Khalid, and Z. Fawaz. 2006. "Numerical and Experimental Investigation of Thermal Signatures of Buried Landmines in Dry Soil." *Journal of Heat Transfer* 128:484–494.

Pan H.L., and L. Mahrt. 1987. "Interaction between Soil Hydrology and Boundary-Layer Development." *Boundary-Layer Meteorology* 38 (1–2):185–202.

Pregowski, P., W. Swiderski, R. T. Walczak, and K. Lamorski. 2000. "Buried Mine and Soil Temperature Prediction by Numerical Model." In *Proceedings of SPIE 4038, Detection and Remediation Technologies for Mines and Minelike Targets V*, 24–28 April, Orlando, FL. https://doi.org/10.1117/12.396227.

Sendur, I. K., and B. A. Baertlein. 2000. "Numerical Simulation of Thermal Signatures of Buried Mines over a Diurnal Cycle." In *Proceedings of SPIE 4038, Detection and Remediation Technologies for Mines and Minelike Targets V*, 24–28 April, Orlando, FL. https://doi.org/10.1117/12.396243.

Simard, J. 1996. "Improved Landmine Detection Capability (ILDC) Systematic Approach to the Detection of Buried Mines Using Passive IR Imaging." *Proceedings of SPIE 2765, Detection and Remediation Technologies for Mines and Minelike Targets*, 8–12 April, Orlando, FL. https://doi.org/10.1117/12.241251.

Sutherland, R. A., J. F. Bartholic, and J. F. Gerber. 1979. "Emissivity Correction for Interpreting Thermal Radiation from a Terrestrial Surface." *Journal of Applied Meteorology and Climatology* 18 (9): 1165–1171.

U.S. Army. 2004. *Mine/Countermine Operations*. FM 20-32, C4.Washington, DC: Department of the Army, Headquarters.

Van Dam, R. L., B. Borchers, J. M. H. Hendrickx, and S. Hong. 2003. "Soil Effects on Thermal Signatures of Buried Nonmetallic Landmines." In *Proceedings SPIE 5089, Detection and Remediation Technologies for Mines and Minelike Targets VIII*, 21–25 April, Orlando, FL. https://doi.org/10.1117/12.487205.

Van De Griend, A. A., P. J. Camillo, and R. J. Gurney. 1985. "Discrimination of Soil Physical Parameters, Thermal Inertia, and Soil Moisture from Diurnal Surface Temperature Fluctuations." *Water Resources Research* 21 (7): 997–1009.

Waldemar, S., P. Hlosta, J. Jarzemski, L. Szugajew, and J. Usowicz. 2012. "Role of Moisture and Density of Sand for Microwave Enhancement of Thermal Detection of Buried Mines." In *Proceedings SPIE 8357, Detection and Sensing of Mines, Explosive Objects, and Obscured Targets XVII*. https://doi.org/10.1117/12.921335.

Wiecek, B., and J. Pacholik. 1995. "Technical Methods of Emissivity Correction in Thermography." *Eurotherm Series* 42:124–130. http://dx.doi.org/10.21611/qirt.1994.021.

Appendix A: Instrumentation Information

Table A-1. Location coordinates, grid location, depth, and naming for the thermocouple sensors.

Sensor Type	Grid Location	Location		Depth cm	Sensor Labels
		Easting	Northing		
BCT	B8/B13	719543.177	4845039.669	0	BCT1
				5.08	BCT2
				15.24	BCT3
				30.48	BCT4
				45.72	BCT5
				60.96	BCT6
BWT	B2/B3	719541.918	4845039.582	0	BCT1
				5.08	BCT2
				15.24	BCT3
				30.48	BCT4
				45.72	BCT5
				60.96	BCT6
BET	B23/B24	719545.041	4845039.99	0	BCT1
				5.08	BCT2
				15.24	BCT3
				30.48	BCT4
				45.72	BCT5
				60.96	BCT6
BST	B15	719543.746	4845038.268	0	BCT1
				5.08	BCT2
				15.24	BCT3
				30.48	BCT4
				45.72	BCT5
				60.96	BCT6
BNT	B21	719544.538	4845041.802	0	BCT1
				5.08	BCT2
				15.24	BCT3
				30.48	BCT4
				45.72	BCT5
				60.96	BCT6

Table A-2. Location coordinates, grid location, depth, and naming for the moisture and temperature sensors.

Sensor Type	Grid Location	Location		Depth cm	Sensor Labels
		Easting	Northing		
Moisture Temp CS655	B13/B18	719543.737	4845039.94	5.08	B1
				15.24	B2
				30.48	B3
				45.72	B4
				60.96	B5
Moisture CS616	NE B21	719545.104	4845041.96	5.08	Soil Moisture #1
				15.24	Soil Moisture #2
				30.48	Soil Moisture #3
				45.72	Soil Moisture #5
Moisture PR2	B10	719543.125	4845038.09	10	PR2_B_10cm
				20	PR2_B_20cm
				30	PR2_B_30cm
				40	PR2_B_40cm
				60	PR2_B_60cm
				100	PR2_B_100cm

Table A-3. Instrumentation and operational parameters used in the study.

Measurement zones	Parameters	Instrument Brand	Unit of Measure	Accuracy
Subsurface	Volumetric water content (VWC) Bulk electrical conductivity Relative dielectric permittivity Temperature	Campbell Scientific CS655	% dS/m dS/m °C	±3% VWC (typical in mineral soils that have solution electrical conductivity ≤ 10 dS/m) ±0.05 dS/m 3% of reading ± 0.8 from 1 to 40 for solution electrical conductivity ≤ 8 dS/m ±0.5°C (for probe body buried in soil)
	VWC	Campbell Scientific CS616	%	±2.5% VWC (using standard calibration with bulk electrical conductivity of ≤0.5 dS/m, bulk density of ≤1.55 g/cm^3, and measurement range of 0% to 50% VWC)
	VWC	Delta-T PR2 probe	%	±4% VWC (0 to 40°C)
	Temperature	CRREL-fabricated thermocouple	°C	±0.2°C (−27°C to 37°C)
Surface and subsurface	Surface heat flux	Campbell Scientific HFP01	Watts/m^2	50 µV/W·m^{-2} (−30°C to 70°C)
Atmospheric	Air temperature	Campbell Scientific HMP60	°C	±0.6°C
	Relative humidity	Campbell Scientific HMP60	%	Typical Accuracy −40°C to 0°C: ±5% (0 to 90 RH%) ±7% (90 to 100 RH%) Typical Accuracy 0°C to 40°C: ±3% (0 to 90 RH%) ±5% (90 to 100 RH%) Typical Accuracy 40°C to 60°C: ±5% (0 to 90 RH%) ±7% (90 to 100 RH%)
	Barometric pressure	Campbell Scientific CS100	mbar	±0.5 hPa (@ +20°C) ±1.0 hPa (@ 0°C to 40°C) ±1.5 hPa (@ −20°C to 40°C) ±2.0 hPa (@ −40°C to 60°C)
	Precipitation	Campbell Scientific TE525WS	mm	1.0% up to 50 mm/h

Measurement zones	Parameters	Instrument Brand	Unit of Measure	Accuracy
	Wind speed	Campbell Scientific 05103	m/sec	±0.3 m/s
	Wind direction	Campbell Scientific 05103	Degrees from north	±3°
	Solar radiation, incoming and reflected (used to calculate surface albedo) (0.285–2.80 µm)	Eppley® Precision Spectral Pyranometer	W/m^2	±2% relative, ±3%–4% absolute accuracy of calibration sensitivity = 9 $\mu V/W \cdot m^{-2}$ linearity = ±0.5% temperature response = 1% (−20°C to 40°C)
Atmospheric and Surface	Visible to near IR (0.295–2.80 µm)	Eppley® Standard Precision Pyranometer	W/m^2	±3.5% accuracy sensitivity = 8 $\mu V/W \cdot m^{-2}$ linearity = ±0.5% temperature response = 0.5% (−30°C to 50°C)
	Soil thermal properties (4–50 µm)	Eppley® Precision Infrared Radiometer	°C	±5% accuracy sensitivity = 3 $\mu V/W \cdot m^{-2}$ linearity = ±0.5% temperature response = 0.5% (−30°C to 50°C)
Surface	Soil thermal properties (7.5–13 µm)	FLIR Systems Inc. A300 with a Scout III 240 lens	°C	±2°C accuracy IR resolution = 320 × 240 pixels, 16-bit temperature range: −15°C to 50°C thermal sensitivity: 0.05°C at 30°C per 50 mK spatial resolution = 1.36 mrad FoV = 24° × 18.8°
Surface	Roughness	Riegl VZ400	mm	5 mm accuracy 3 mm precision 800 m range FoV = 100° vertical/360° horizontal

REPORT DOCUMENTATION PAGE

Form Approved
OMB No. 0704-0188

1. REPORT DATE (DD-MM-YYYY)	2. REPORT TYPE	3. DATES COVERED (From - To)
August 2020	Technical Report / Final	FY16–FY17

4. TITLE AND SUBTITLE
Spatial and Temporal Variance in the Thermal Response of Buried Objects

5a. CONTRACT NUMBER

5b. GRANT NUMBER

5c. PROGRAM ELEMENT
622784

6. AUTHOR(S)
Jay L. Clausen, Jason R. Dorvee, Anna Wagner, Susan Frankenstein, Blaine F. Morriss, Keran J. Claffey, Terrance M. Sobecki, Christopher R. Williams, Stephen D. Newman, Brandon K. Booker, Rosa T. Affleck, Charles E. Smith, Michele L. Maxson, Andrew P. Bernier, and Bonnie J. Jones

5d. PROJECT NUMBER
T40

5e. TASK NUMBER
A1040

5f. WORK UNIT NUMBER

7. PERFORMING ORGANIZATION NAME(S) AND ADDRESS(ES)
U.S. Army Engineer Research and Development Center (ERDC)
Cold Regions Research and Engineering Laboratory (CRREL)
72 Lyme Road
Hanover, NH 03755-1290

8. PERFORMING ORGANIZATION REPORT NUMBER
ERDC/CRREL TR-20-10

9. SPONSORING / MONITORING AGENCY NAME(S) AND ADDRESS(ES)
U.S. Army
Communications-Electronics Research, Development, and Engineering Center Night Vision and Electronic Sensors Directorate
Fort Belvoir, VA 22060

10. SPONSOR/MONITOR'S ACRONYM(S)

11. SPONSOR/MONITOR'S REPORT NUMBER(S)

12. DISTRIBUTION / AVAILABILITY STATEMENT
Approved for public release; distribution is unlimited.

13. SUPPLEMENTARY NOTES

14. ABSTRACT

Probability of detection and false alarm rates for current military sensor systems used for detecting buried objects are often unacceptable. One approach to increasing sensor performance and detection reliability is to better understand which physical processes are dominant under certain environmental conditions. Incorporating this understanding into detection algorithms will improve detection performance.

Our approach involved studying a small, 3.05 × 3.05 m, test plot at the Engineer Research and Development Center's Cold Regions Research and Engineering Laboratory (ERDC-CRREL) in Hanover, New Hampshire. There we monitored a number of environmental variables (soil temperature moisture, and chemistry as well as air temperature and humidity, cloud cover, and incoming solar radiation) coupled with thermal infrared and electro-optical image collection. Data collection occurred over 4 months with measurements made at 15 minute intervals.

Initial findings show that significant spatial and thermal temporal variability is caused by incoming solar radiation; meteorologically driven surface heat exchange; and subsurface-soil temperatures, density, moisture content, and surface roughness.

15. SUBJECT TERMS
Detectors, Earth temperature, Environmental conditions, Infrared detectors, Military surveillance, Soil moisture, Soils--Density, Soils--Thermal properties

16. SECURITY CLASSIFICATION OF:			17. LIMITATION OF ABSTRACT	18. NUMBER OF PAGES	19a. NAME OF RESPONSIBLE PERSON
a. REPORT	b. ABSTRACT	c. THIS PAGE			19b. TELEPHONE NUMBER (include area code)
Unclassified	Unclassified	Unclassified	SAR	65	